



Segmentation of the Tashkurgan normal fault in the eastern Pamir: Insights from geomorphology and thermochronology and implications for fault-slip transfer

Journal Article**Author(s):**

Chen, Shenqiang; Fellin, Maria Giuditta; Willett, Sean D.; Maden, Colin ; Guillong, Marcel ; Chen, Hanlin; Chen, Yaguang; Yang, Rong

Publication date:

2024-05-10

Permanent link:

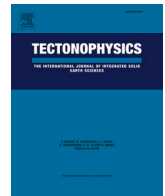
<https://doi.org/10.3929/ethz-b-000668671>

Rights / license:

[Creative Commons Attribution 4.0 International](#)

Originally published in:

Tectonophysics 878, <https://doi.org/10.1016/j.tecto.2024.230305>



Segmentation of the Tashkurgan normal fault in the eastern Pamir: Insights from geomorphology and thermochronology and implications for fault-slip transfer

Shenqiang Chen^{a,c,*}, Maria Giuditta Fellin^a, Sean D. Willett^a, Colin Maden^a, Marcel Guillong^a, Hanlin Chen^b, Yaguang Chen^b, Rong Yang^b

^a Department of Earth Sciences, ETH Zurich, 8092 Zurich, Switzerland

^b School of Earth Sciences, Zhejiang University, 310027 Hangzhou, China

^c Now at Institute of Geology, Chinese Academy of Geological Sciences, 100037 Beijing, China

ARTICLE INFO

Keywords:

Pamir
Normal faulting
Geomorphology
Thermochronology
Thermokinematic modeling

ABSTRACT

At the northwestern end of the India–Asia collision zone, in the eastern Pamir interior, the Kongur Shan extensional system extends for ~250 km as a composite system of normal faults. As the southernmost segment of the extensional system, the Tashkurgan fault can be divided into a northern and southern segment by the intersection of the Tahman and Tashkurgan faults. To evaluate the tectonic activity along the Tashkurgan fault and explore the extensional characteristics of the southern Kongur Shan extensional system, we integrate geomorphologic analysis with thermochronologic data and modeling. Geomorphic indices, including local relief, normalized channel steepness index (k_{sn}), and river χ -plots, show that the southern Tashkurgan fault is more active than the northern Tashkurgan fault. On the footwall of the northern Tashkurgan fault, most thermochronologic data, which include biotite $^{40}\text{Ar}/^{39}\text{Ar}$ (Arbt), zircon (U-Th)/He (ZHe), apatite fission track (AFT), and apatite (U-Th-Sm)/He (AHe) dates, record emplacement-related cooling, and only a few AHe dates possibly record exhumation of <2 km since ~7 Ma ago. On the footwall of the southern Tashkurgan fault, almost all of the ZHe, AFT, and AHe dates record significant late Miocene to present exhumation; thus, we perform three-dimensional thermokinematic modeling for the normal slip along this fault segment. Modeling results indicate a probably constant slip rate on the southern Tashkurgan fault at a value of 1.4–1.5 mm/a, which corresponds to 6–7 km of both horizontal extension and footwall uplift since 6.5 Ma ago. All together, the geomorphic and thermochronologic evidences imply that the southern Tashkurgan fault is responsible for the ~E–W extension along the southernmost portion of the Kongur Shan extensional system, while the northern fault segment plays a minor role in the extension. This result, combined with the previously published magnitude of extension along the southern Kongur Shan fault, indicates that the extension at any site along the southern Kongur Shan extensional system can be primarily attributed to normal faulting along a single border fault, which is a typical characteristic of an interbasin transfer zone with a transfer fault.

1. Introduction

Late Cenozoic extensional systems are widely distributed in the Himalayan–Tibetan orogen (Yin and Harrison, 2000; Mitsuishi et al., 2012; Bian et al., 2020). As the western prolongation of the continent–continent collisional orogen (Fig. 1a), the Pamir salient also experienced crustal extension which resulted in exhumation of gneiss domes (Fig. 1b; Robinson et al., 2004, 2007; Cao et al., 2013a, 2013b; Stearns et al., 2013, 2015; Stübner et al., 2013a, 2013b; Thiede et al.,

2013; Rutte et al., 2017a, 2017b; Worthington et al., 2020; Chen et al., 2023). Late Miocene to present tectonic activity in the eastern Pamir is characterized by thrusting and strike-slip movement along the front and ~E–W extension in the interior, where the ~250 km-long Kongur Shan extensional system bounds extensional ranges that include the highest peaks of the Pamir (Robinson et al., 2004, 2007; Cowgill, 2010; Sobel et al., 2011, 2013; Cao et al., 2013a, 2013b; Thiede et al., 2013; Cai et al., 2017; Chen and Chen, 2020; Chen et al., 2023).

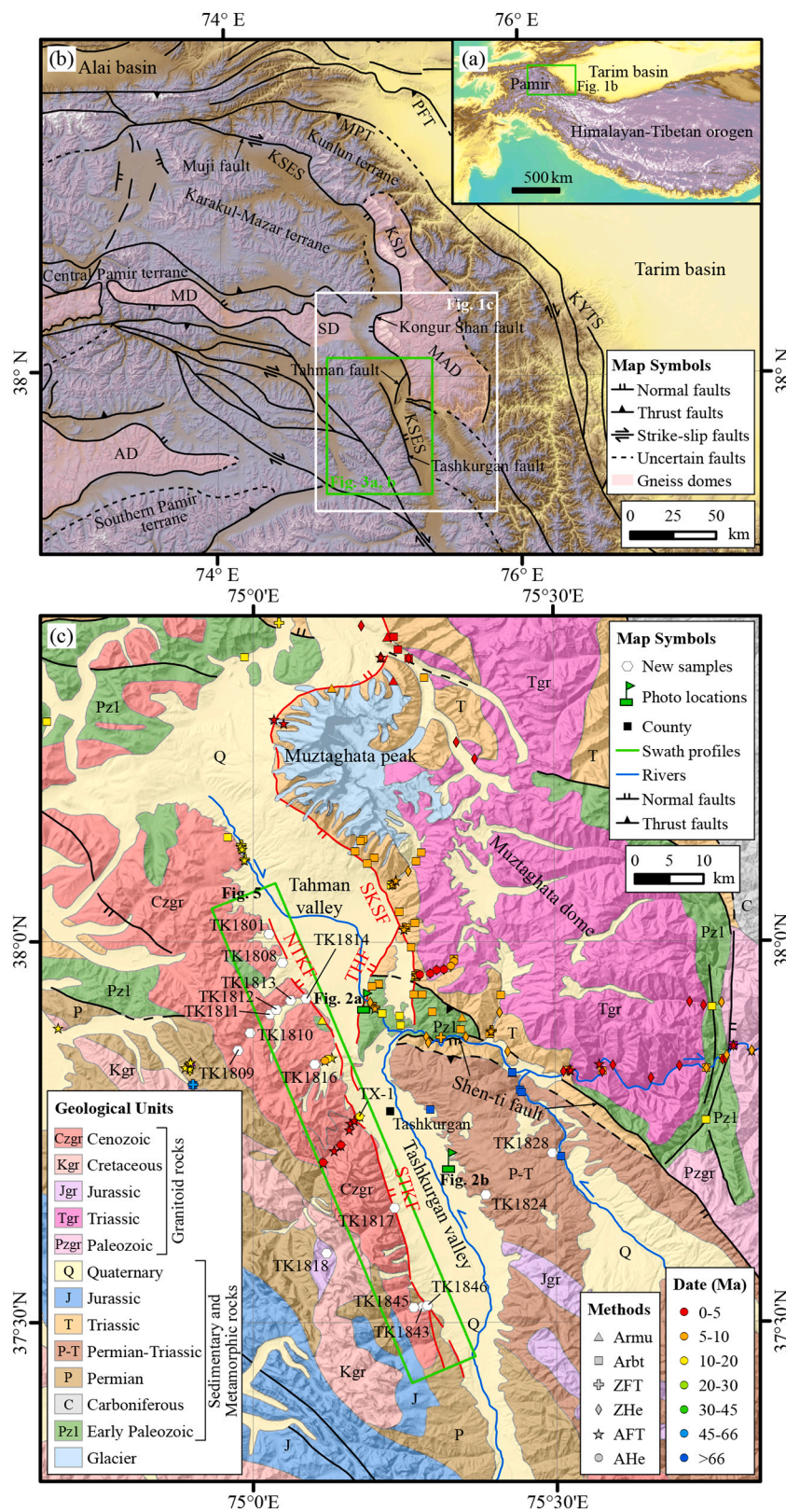
* Corresponding author at: Department of Earth Sciences, ETH Zurich, 8092 Zurich, Switzerland.
E-mail address: geocsq@163.com (S. Chen).

<https://doi.org/10.1016/j.tecto.2024.230305>

Received 27 September 2023; Received in revised form 31 March 2024; Accepted 1 April 2024

Available online 2 April 2024

0040-1951/© 2024 The Authors. Published by Elsevier B.V. This is an open access article under the CC BY license (<http://creativecommons.org/licenses/by/4.0/>).



(caption on next page)

Fig. 1. (a) The eastern portion of the Pamir salient in the India–Asia collision zone. (b) Tectonic overview of the eastern Pamir with late Cenozoic gneiss domes and major faults (the location is shown in Fig. 1a). Modified from Schmidt et al. (2011), Sobel et al. (2013), and Thiede et al. (2013). AD: Alichur dome; KSD: Kongur Shan dome; KSES: Kongur Shan extensional system; KYTS: Kashgar–Yecheng transfer system; MAD: Muztaghata dome; MD: Muskol dome; MPT: Main Pamir thrust; PFT: Pamir Frontal thrust; SD: Shatput dome. (c) Geological map of the southern portion of the Kongur Shan extensional system and adjacent area showing distribution of lithologic ages, faults, thermochronologic dates, and new samples in this study (the location is shown in Fig. 1b). Modified from Robinson et al. (2007, 2012), Cai et al. (2017), and Chen et al. (2023). Thermochronologic data are compiled from Robinson et al. (2007), Sobel et al. (2011, 2013), Cao et al. (2013a), Thiede et al. (2013), Cai et al. (2017, 2020, 2021), Rutte et al. (2017b), Chen and Chen (2020), and Chen et al. (2023). Our new samples are shown by white hexagons with labels. The green rectangle represents the location of a swath profile. NTKF: northern Tashkurgan fault; SKSF: southern Kongur Shan fault; STKF: southern Tashkurgan fault; THF: Tahman fault; Armu: muscovite $^{40}\text{Ar}/^{39}\text{Ar}$; Arbt: biotite $^{40}\text{Ar}/^{39}\text{Ar}$; ZFT: zircon fission track; ZHe: zircon (U–Th)/He; AFT: apatite fission track; AHe: apatite (U–Th–Sm)/He. (For interpretation of the references to colour in this figure legend, the reader is referred to the web version of this article.)

The Kongur Shan extensional system consists of several fault segments that in the south include the Tashkurgan normal fault (Fig. 1b; Robinson et al., 2004, 2007; Thiede et al., 2013; Chen and Chen, 2020; Wu et al., 2023). The Tashkurgan fault dips to the NEE and is connected to the W-dipping southern Kongur Shan normal fault through a transfer structure, namely the NW-dipping Tahman normal fault (Fig. 1c; Robinson et al., 2007; Wu et al., 2023). The intersection of the Tashkurgan and Tahman faults divides the Tashkurgan fault into a northern and southern segment. Both segment footwalls expose Miocene granitic rocks that were the focus of a previous thermochronologic study (Chen and Chen, 2020), which estimated the onset timing of slip along the southern Tashkurgan fault (10–5 Ma) and the average exhumation rate for the footwall of the southern segment (0.6–0.9 mm/a in the past ~5 Ma). This initiation age was roughly constrained by the youngest thermochronologic date from the hanging wall and the oldest date from the footwall, and this exhumation rate was simply calculated by a one-dimensional analytical method. The activity of the northern Tashkurgan fault has remained unconstrained due to the overlap between cooling and intrusion ages (Cai et al., 2020; Chen and Chen, 2020). ^{10}Be -derived erosion rates in the catchments along the footwall of the Tashkurgan fault indicate that during the past several thousand years, the southern fault segment was more active than the northern one (Wu et al., 2023). However, it is necessary to provide more evidence to further constrain the long-term tectonic activity along the two segments of the Tashkurgan fault.

In this contribution, we take advantage of remarkable landscape features and thermochronologic data along the strike of the Tashkurgan fault to provide new constraints on its activity. To obtain the slip rate on the southern segment of the Tashkurgan fault, we integrate our new zircon (U–Th)/He (ZHe) and apatite (U–Th–Sm)/He (AHe) dates with previous data from the footwall of the fault segment, and then compare them with the predictions made from the three-dimensional (3-D) thermokinematic model Pecube (Braun, 2003; Braun et al., 2012). Our results help quantify the characteristics of fault-slip transfer in the southern portion of the Kongur Shan extensional system and provide further constraints on the processes that control crustal deformation in the eastern Pamir.

2. Background

The Pamir salient defines the northwestern end of the India–Asia collision zone and is bounded by the Main Pamir thrust to the north and by the Kashgar–Yecheng transfer system to the east (Fig. 1a, b). During the Cenozoic, tectonic deformation has been superimposed onto the terranes that comprise the Pamir salient and were accreted during the late Paleozoic to early Mesozoic (Burtman and Molnar, 1993; Burtman, 2010; Robinson et al., 2012; Robinson, 2015; Angiolini et al., 2013; Villarreal et al., 2020; Chen et al., 2021; Li et al., 2022; Rembe et al., 2022). The Pamir interior has absorbed >300 km (Burtman and Molnar, 1993) or > 80–90 km (Robinson, 2015; Rutte et al., 2017a) of Cenozoic crustal shortening. Rapid footwall exhumation along normal faults at the boundary of gneiss domes has resulted in the exposure of igneous and medium- to high-grade metamorphic middle–lower crustal rocks (Robinson et al., 2004, 2007; Stübner et al., 2013a, 2013b; Stearns et al., 2013, 2015; Rutte et al., 2017a, 2017b; Worthington et al., 2020; Chen et al., 2023).

In the eastern Pamir, the Kongur Shan extensional system bounds the Kongur Shan and Muztaghata gneiss domes that expose deep crustal rocks (Fig. 1b; Robinson et al., 2004, 2007; Cai et al., 2017; Li et al., 2020). The magnitude of horizontal extension along the extensional system decreases southward from 30–35 km at the Kongur Shan dome (Robinson et al., 2007), to ~20 km at the Muztaghata peak (Robinson et al., 2007), and finally to 8–9 km along the southern end of the Kongur Shan fault (Chen et al., 2023). In the southernmost portion of the Kongur Shan extensional system, Miocene granitoid rocks are exposed on the footwall of the Tashkurgan normal fault, and they were intruded into composite host rocks including Paleozoic–Mesozoic sedimentary and metamorphic rocks and Cretaceous granitoids (Fig. 1c; Robinson et al., 2007, 2012; Jiang et al., 2012; Tang et al., 2022). For the Miocene granitoids from the footwall of the southern Tashkurgan fault, the Al-in-amphibole barometer yielded crystallization pressures of 1.48–1.56 kbar indicating an emplacement depth of ~5 km (Jiang et al., 2012).

The southern Kongur Shan fault defines the eastern boundary of the Tahman valley, and the northern and southern Tashkurgan fault segments respectively define the western boundaries of the Tahman and Tashkurgan valleys (Fig. 1c). These two valleys sit at elevations ranging from 3100 m to 3500 m, trend NNW–SSE, have slopes that rise up to elevations over 4000 m and locally over 6000 m, and are filled by Quaternary glacial, alluvial, and fluvial deposits (Robinson et al., 2007; Owen et al., 2012; Imreke et al., 2019). The western slopes of the Tahman valley and of the Tashkurgan valley are the footwalls of the northern and southern Tashkurgan fault, respectively. The southern Tashkurgan fault features triangular facets with an average dip angle of ~45° (Fig. 2b). The last glacial stage on the footwall of the southern Tashkurgan fault likely occurred at 20 ± 4 ka (standard deviation: sd) (Owen et al., 2012), after which only the highest portions of the footwall were covered by glaciers.

3. Methods

3.1. Geomorphic analysis

Geomorphic indices, such as local relief, normalized channel steepness index (k_{sn}), and χ , are correlated with tectonic uplift and river erosion rates, and they provide snapshots of these dynamics (Snyder et al., 2000; Burbank and Anderson, 2012; Kirby and Whipple, 2012; Perron and Royden, 2013; Willett et al., 2014). We use these proxies to reveal how the landscape varies along the Tashkurgan fault in response to fault activity. Towards this goal, we extracted a local relief map, k_{sn} values, and river χ -plots from the three arc-second (90 m resolution) Shuttle Radar Topography Mission digital elevation model (SRTM DEM) data using TopoToolbox (Schwanghart and Kuhn, 2010; Schwanghart and Scherler, 2014).

Topographic relief is defined as the difference between the maximum and minimum elevations of a local area. An extensional footwall with a rapid uplift rate is characterized by a linear mountain front with high local relief (Burbank and Anderson, 2012). Thus, the relief in a normal-faulted range front can be used to evaluate the relative tectonic activity along the normal fault. In this study, the local relief was calculated within a radius of 500 m.

The channel steepness index (k_s) is defined as a power-law function of local channel slope (S) and upstream drainage area (A):

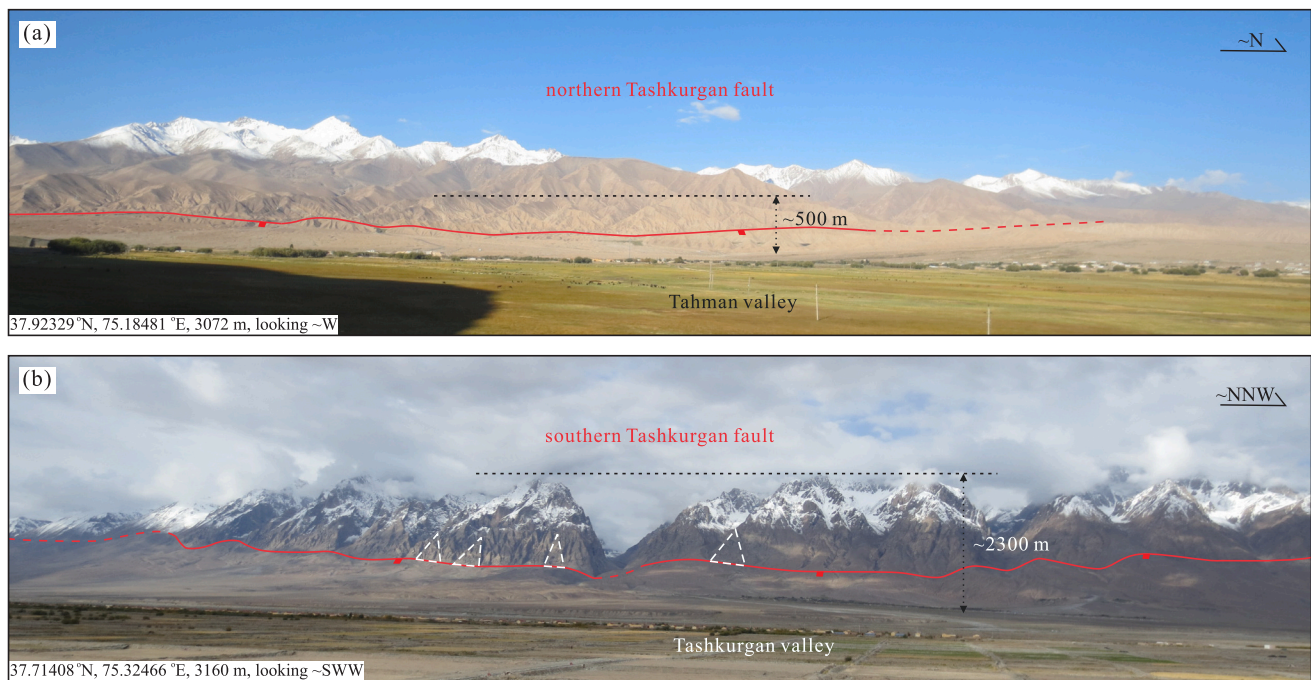


Fig. 2. Field photos show geomorphologic features along (a) the northern Tashkurgan fault and (b) the southern Tashkurgan fault (the photo locations are shown in Fig. 1c). The red lines represent the surface trace of the Tashkurgan fault. The horizontal dashed black lines roughly represent the highest elevations along the fault (<5 km away from the fault). The vertical dotted black lines with two arrows show the elevation differences across the fault. The dashed white triangles represent triangular facets along the fault. (For interpretation of the references to colour in this figure legend, the reader is referred to the web version of this article.)

$$k_s = S \times A^\theta \quad (1)$$

where θ is the channel concavity index (Snyder et al., 2000; Kirby and Whipple, 2012). A positive correlation between k_s and rock uplift rate has been reported in Wobus et al. (2006). To compare k_s from river channels with different θ , we extracted normalized channel steepness index (k_{sn}) using a typical reference concavity (θ_{ref}) of 0.45 (Wobus et al., 2006; Kirby and Whipple, 2012).

The quantity χ is an integral function of position and can be calculated along a channel from the outlet (x_b) to the location of interest (x) by

$$\chi = \int_{x_b}^x \left(\frac{A_0}{A(x)} \right)^{\theta_{ref}} dx' \quad (2)$$

where A is the upstream drainage area, A_0 is an arbitrary scaling area, and θ_{ref} is a reference concavity (Perron and Royden, 2013). A steady state channel with uniform rock uplift rate, rock erodibility, and precipitation rate should have a linear plot of χ versus channel elevation (Willett et al., 2014). Here, we used an A_0 value of 1 m^2 and a θ_{ref} value of 0.45 to measure the χ values.

3.2. Thermochronometric analysis

We collected 16 bedrock samples at different sites distributed along the southern portion of the Kongur Shan extensional system, including nine samples from the footwall of the northern Tashkurgan fault, five samples from the footwall of the southern Tashkurgan fault, and two samples from the eastern side of the Tashkurgan valley (Fig. 1c; Table 1).

Apatite and zircon grains were extracted from crushed samples using conventional methods of heavy liquid and magnetic separation. Euhedral grains, free of inclusions for apatites and free of fractures for apatites and zircons, were selected and photographed to measure their dimensions under a polarized stereoscope at a high magnification of 160 \times . Apatites of sufficient quality for thermochronologic dating were

obtained from 13 samples and zircons from 15 samples. The grain dimensions can be used to calculate two alpha-ejection correction factors: (1) F_{TK} for homogenous U-Th distributions following Ketchum et al. (2011), and (2) F_{TZ} for zoned U-Th distributions based on U-Th concentration depth-profiles following Hourigan et al. (2005). U-Th contents are usually heterogenous both in apatites and zircons. However, U-Th concentrations in zircons could vary over orders of magnitudes, while the concentrations in apatites are typically low (<100 ppm) resulting in small variations within single grains and negligible effects on the alpha-ejection correction. Thus, we derived F_{TK} values for apatites and F_{TK} and F_{TZ} values for zircons. The U-Th concentration depth-profiles were measured via laser ablation inductively coupled plasma-mass spectrometer (ICP-MS) for all dated zircons with a laser spot size of 30 μm in diameter. The analytical spots are located at the centers of the unpolished zircons. The laser pits have depths of 35–40 μm , which are approximately half-widths of the zircons. We also obtained U-Pb dates for the zircon grains from the laser ablation ICP-MS analysis.

Zircon U-Th-Pb, apatite (U-Th-Sm)/He (AHe), and zircon (U-Th)/He (ZHe) analyses were conducted at ETH Zurich, Switzerland, following the analytical procedures given in Chen et al. (2023). The Helium-4 (^4He) concentration of each grain was determined by outgassing with a diode laser at high temperatures (910 $^\circ\text{C}$ for apatites and 1090 $^\circ\text{C}$ for zircons) and measuring the released gas on a sector-field noble gas MS in static vacuum. Several re-extractions were performed until the fraction of ^4He from the last extraction was <1%. Outgassed grains were transferred into Teflon vials, spiked with mixed U-Th-Sm/U-Th solution, and dissolved. U and Th concentrations, and Sm for apatites, of each final solution were measured on an ICP-MS (Element XR). Effective U ($eU = U + 0.235 \times \text{Th}$; Gautheron et al., 2009, 2013) concentration of each grain, which is a proxy for radiation damage, was determined from the whole-grain solution measurement.

Six fragments from the standard Durango were processed together with our apatite samples. One fragment was lost during the analysis, while the other five fragments yielded a mean F_{TK} -corrected AHe date of $31.9 \pm 0.7 \text{ Ma}$ (sd), where the uncertainty refers to the one standard deviation of the mean (Table S1 in the supplementary material), and

Table 1
Summary of new apatite and zircon (U-Th)/He data.

Sample	Longitude (°E)	Latitude (°N)	Elevation (m)	Lithology	Fault footwall ^a	Method ^b	F _T K date ± sd (Ma) ^c	F _T Z date ± sd (Ma) ^c	Comments
TK1801	75.0260	38.0111	3499	granitoid	NTKF	AHe	9.05 ± 1.07		Average of 3 aliquots
						ZHe	9.72 ± 1.11	8.94 ± 1.31	Average of 4 aliquots
TK1808	75.0481	37.9735	3578	granitoid	NTKF	AHe	8.24 ± 1.48		Average of 5 aliquots
						ZHe	8.35 ± 0.76	8.10 ± 0.38	Average of 5 aliquots
TK1809	74.9742	37.8584	4270	granitoid	NTKF	AHe	9.64 ± 1.49		Average of 5 aliquots
						ZHe	8.84 ± 0.93	9.08 ± 1.68	Average of 5 aliquots
TK1810	74.9949	37.8810	4105	granitoid	NTKF	AHe	7.49 ± 0.03		1 aliquot
						ZHe	10.6 ± 0.2	9.59 ± 0.26	Average of 4 aliquots
TK1811	75.0270	37.9057	3831	granitoid	NTKF	AHe	6.05 ± 0.95		Average of 5 aliquots
						ZHe	9.48 ± 0.68	8.92 ± 0.45	Average of 5 aliquots
TK1812	75.0381	37.9121	3743	granitoid	NTKF	AHe	7.92 ± 1.29		Average of 3 aliquots
						ZHe	8.97 ± 0.68	9.04 ± 0.44	Average of 5 aliquots
TK1813	75.0618	37.9244	3626	granitoid	NTKF	AHe	9.30 ± 0.52		Average of 5 aliquots
						ZHe	9.72 ± 0.26	9.10 ± 0.53	Average of 5 aliquots
TK1814	75.0874	37.9262	3481	granitoid	NTKF	AHe	8.80 ± 0.38		Average of 4 aliquots
						ZHe	9.20 ± 0.88	9.48 ± 1.44	Average of 5 aliquots
TK1816	75.1017	37.8400	3830	granitoid	NTKF	AHe	7.06 ± 2.35		Average of 5 aliquots
						ZHe	9.46 ± 1.07	9.47 ± 0.79	Average of 4 aliquots
TK1817	75.2333	37.6513	3558	granitoid	STKF	AHe	2.43 ± 0.56		Average of 5 aliquots
						ZHe	4.31 ± 0.56	3.96 ± 0.32	Average of 5 aliquots
TK1818	75.1207	37.5916	4685	granitoid	STKF	AHe	7.76 ± 0.24		Average of 5 aliquots
						ZHe	12.0 ± 0.7	11.8 ± 0.3	Average of 5 aliquots
TK1824	75.3842	37.6685	3427	gneiss	/	ZHe	10.7 ± 0.5	10.5 ± 0.7	Average of 5 aliquots
TK1828	75.4947	37.7231	3152	granitoid gneiss	/	ZHe	11.6 ± 1.2	11.1 ± 1.4	Average of 5 aliquots
TK1843	75.2791	37.5220	3659	granitoid	STKF	AHe	3.20 ± 1.28		Average of 2 aliquots
						ZHe	4.70 ± 0.77	4.37 ± 0.75	Average of 5 aliquots
TK1845	75.2635	37.5197	3716	granitoid	STKF	AHe	1.21 ± 0.39		Average of 4 aliquots
TK1846	75.2870	37.5233	3634	granitoid	STKF	ZHe	4.90 ± 0.92	5.01 ± 1.01	Average of 5 aliquots

Analytical details of the measurements are shown in Tables S1 and S2.

^a NTKF is the northern Tashkurgan fault; STKF is the southern Tashkurgan fault.

^b AHe is apatite (U-Th-Sm)/He; ZHe is zircon (U-Th)/He.

^c F_TK and F_TZ are alpha ejection factors after Ketcham et al. (2011) and Hourigan et al. (2005), respectively. sd is the one standard deviation of each mean date. Bold dates were selected.

which is in good agreement with the reference date of 31.0 ± 1.0 Ma (sd) (McDowell et al., 2005). 12 zircons from the Fish Canyon Tuff were processed together with our zircon samples and yielded a mean $^{206}\text{Pb}/^{238}\text{U}$ date of 27.8 ± 0.6 Ma (sd), a mean F_TK-corrected ZHe date of 27.9 ± 1.0 Ma (sd), and a mean F_TZ-corrected ZHe date of 26.7 ± 1.3 Ma (sd) (Tables S2 and S3), which are consistent with an eruption age of 28.2–28.0 Ma (Boehnke and Harrison, 2014).

4. Results

4.1. Geomorphic results

4.1.1. Local relief

Along the western slope of the Tahman valley, the local relief within ~5 km from the northern Tashkurgan fault (i.e., the mountain front along the northern segment) is generally <400 m, while along the western slope of the Tashkurgan valley, the relief within ~5 km from the

southern Tashkurgan fault (i.e., the mountain front along the southern segment) is generally >600 m and locally >1000 m (Fig. 3a).

4.1.2. Normalized channel steepness index (k_{sn})

We extracted four drainage basins (i.e., 1–4) from the footwall of the northern Tashkurgan fault and another four basins (i.e., 5–8) from the footwall of the southern segment (Fig. 3a, b). On the footwall of the northern Tashkurgan fault, the normalized channel steepness index (k_{sn}) values within ~5 km from the northern segment (i.e., the mountain front along the segment) are <300 or even <200, whereas on the footwall of the southern Tashkurgan fault, within ~5 km from the southern segment (i.e., the mountain front along the segment), the k_{sn} values of about half of the channels are >300 (Fig. 3b). Moreover, more than half of the upstream channels in drainage basin 5 have low k_{sn} values of <100.

4.1.3. River χ -plots

The χ -elevation profiles for the trunk channels in drainage basins 1–4 are much closer to straight lines than the profiles for the trunk channels in basins 5–8 (Fig. 4). Especially for the trunk channel in drainage basin 5, its upper reach has a lower slope than its lower reach, and three knickpoints have been observed (Figs. 3b and 4).

4.2. Thermochronometric results

4.2.1. Apatite (U-Th-Sm)/He results

The results of the (U-Th-Sm)/He dating of our apatites are presented in Tables 1 and S1. Two apatites (TK1810a3 and TK1814a3) were lost during the analysis. AHe dates (73–13 Ma) from five apatites (TK1801a1, TK1801a2, TK1810a1, TK1812a3, and TK1812a5) are older than the intrusion age (12–10 Ma) of the sampled pluton (Robinson et al., 2007; Jiang et al., 2012; Tang et al., 2022), and AHe dates from

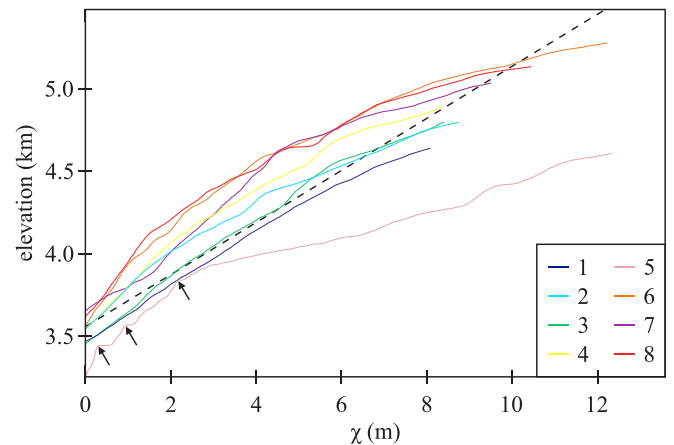


Fig. 4. Normalized distance-elevation plots (χ -plots) for the trunk channels of drainage basins on the footwall of the Tashkurgan fault. The locations of the drainage basins and their trunk channels are shown in Fig. 3a. The dashed straight line is the reference line representing a steady state channel. The black arrows point to the knickpoints along the trunk channel of drainage basin 5.

two apatites (TK1843a1 and TK1845a2) are older than their corresponding mean ZHe dates. We have no control on the factors that could explain the relatively old AHe dates as, for instance, grain composition and U-Th zoning, which can affect helium distribution and diffusion kinetics. Therefore, we discard these nine AHe dates from 61 dated apatites. The mean AHe date and its standard deviation of each sample were calculated after removing the outlier grain dates.

On the footwall of the northern Tashkurgan fault, samples TK1801, TK1808–TK1814, and TK1816 yield nine mean AHe dates of 9.6–6.0 Ma. One of these samples (TK1810) includes only one single-grain AHe date.

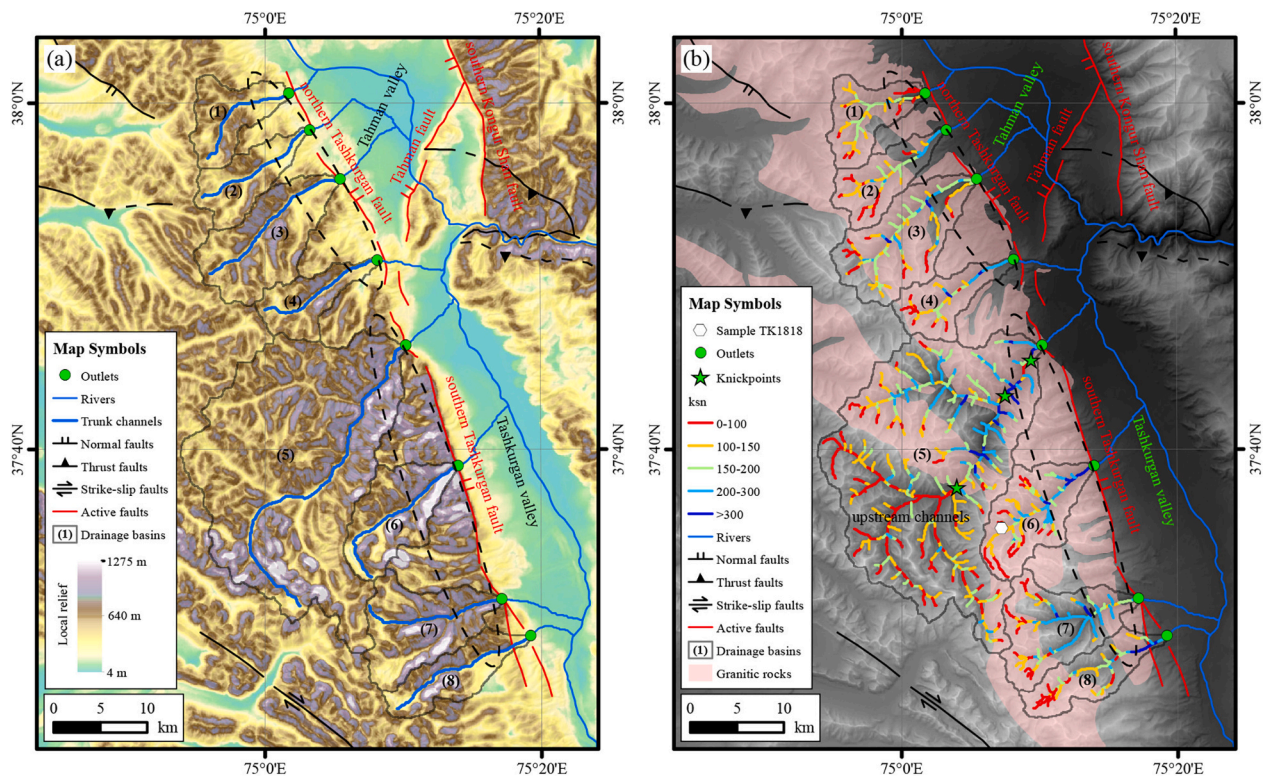


Fig. 3. (a) Local relief map of the footwall and hanging wall of the Tashkurgan fault and adjacent area with faults and rivers. (b) Normalized channel steepness (k_{sn}) map of main drainage basins on the footwall of the Tashkurgan fault. The drainage basins are labeled by numbers. The location of the maps is shown in Fig. 1b. The ellipses with dashed black outlines roughly circle the mountain fronts along the northern and southern Tashkurgan fault segments (i.e., within ~5 km from the segments).

Sample TK1816 includes five single-grain dates with a high dispersion reflected by the one standard deviation (sd) value of 2.4 Ma, corresponding to a relative value of 33%. The remaining samples from the footwall of the northern fault segment contains three to five single-grain dates with low-to-medium dispersions as attested by their sd values of 0.4–1.5 Ma, corresponding to relative values of 4%–18%. On the footwall of the southern Tashkurgan fault, samples TK1817, TK1843, and TK1845 give three mean AHe dates of 3.2–1.2 Ma, while sample TK1818 yields a relatively old AHe date of 7.8 ± 0.2 Ma (sd). One of these four samples (TK1843) includes only two single-grain AHe dates (4.1 Ma and 2.3 Ma), which are quite apart from each other. The remaining samples from the footwall of the southern segment include four or five single-grain dates with sd values of 0.2–0.6 Ma, corresponding to relative values of 3%–33%. The youngest sample (TK1845) has the highest relative dispersion.

All the acceptable apatites excepting one grain from sample TK1808 give low-to-medium eU concentrations of 9–65 ppm. F_TK -corrected single-grain AHe date-versus-eU content plot shows positive correlations for samples TK1801, TK1812, and TK1814 and a negative correlation for sample TK1818 (Fig. S1a). The remaining samples show no correlation between AHe dates and eU contents.

4.2.2. Zircon U-Th-Pb results

The U-Th concentration depth-profiles of our zircon grains are shown in Fig. S2. The U and Th concentrations are variable along the profile in each zircon, and they show strong changes in most grains. The Th/U ratio is also variable along the depth-profiles of the grains. Five zircons from sample TK1828 give Th/U ratios <0.1 along the entire depth-profiles, indicating that they could be of metamorphic origin; some zircons (e.g., TK1811z1, TK1813z3, TK1814z5, TK1818z3, and TK1846z1) could have experienced metamorphism because they have very low Th/U ratios (<0.1) in the interior; but most zircons have Th/U ratios >0.1 , indicating that they are likely to be of igneous origin (Hidaka et al., 2002).

Most zircons from samples TK1801, TK1808–TK1814, TK1816, TK1817, TK1843, and TK1846, which were collected from the Miocene pluton, yield $^{206}Pb/^{238}U$ dates of 15.4–9.8 Ma that are consistent with the reported intrusion age (12–10 Ma) of the pluton (Robinson et al., 2007; Jiang et al., 2012; Tang et al., 2022) within the range of uncertainty (Table S3). Some zircons from the pluton (e.g., TK1801z2, TK1801z5, TK1808z2, TK1812z4, TK1814z3, TK1816z1, and TK1817z2) give relatively old U-Pb dates of 791–37 Ma, which could represent inherited dates. In addition, zircons from samples TK1818, TK1824, and TK1828 yield late Triassic–early Jurassic U-Pb dates.

4.2.3. Zircon (U-Th)/He results

The results of the (U-Th)/He dating of our zircons are given in Tables 1 and S2. The U-Th concentration-depth variations, especially in zircons TK1809z2, TK1812z2, TK1813z2, TK1814z2, TK1817z5, TK1828z2, TK1843z5, and TK1846z1, have effects on the alpha-ejection correction factors (F_TK versus F_TZ) and on the final ZHe dates (F_TK date versus F_TZ date). We found $<20\%$ relative differences in the alpha-ejection correction factors, which result in $<17\%$ relative date differences (i.e., <1.6 Ma date differences). Herein we used the F_TZ -corrected dates for our dated zircons.

F_TZ -corrected ZHe dates of zircons TK1801z5, TK1810z3, and TK1816z2 range from 24 Ma to 14 Ma, and they are older than the intrusion age (12–10 Ma) of the Miocene pluton (Robinson et al., 2007; Jiang et al., 2012; Tang et al., 2022); thus, these three single-grain dates out of 75 dated zircons are discarded. The mean ZHe date and its standard deviation (sd) of each sample were calculated after removing the outlier single-grain dates. In all samples, the sd values vary between 0.3 Ma and 1.7 Ma, corresponding to relative values of 3% to 20%, indicating that our ZHe dates have low-to-medium dispersions. Samples (TK1801, TK1808–TK1814, and TK1816) from the footwall of the northern Tashkurgan fault yield nine mean ZHe dates of 9.6–8.1 Ma,

which are younger than the emplacement age of the samples. On the footwall of the southern Tashkurgan fault, samples TK1817, TK1843, and TK1846 yield three mean ZHe dates of 4.9–4.3 Ma, while sample TK1818 yields a relatively old ZHe date of 11.8 ± 0.3 Ma (sd). Two samples (TK1824 and TK1828) from the eastern side of the Tashkurgan valley give two mean ZHe dates of 10.5 ± 0.7 Ma (sd) and 11.1 ± 1.4 Ma (sd).

All the acceptable zircon grains yield low-to-high eU contents of 374–4833 ppm, and most of the grains have eU concentrations of <3000 ppm. F_TZ -corrected single-grain ZHe date-versus-eU content plot shows negative correlations for samples TK1813 and TK1828 (Fig. S1b).

5. Interpretations of the thermochronologic data

5.1. Cooling dates from the footwall of the northern Tashkurgan fault

Previous biotite $^{40}Ar/^{39}Ar$ (Arbt), apatite fission track (AFT), and AHe dates (i.e., 11–10 Ma from samples 9.10.10.10G, 10.10.10.10G, 11.10.10.10G, and XK4-1-8) from the footwall of the northern Tashkurgan fault overlap with the intrusion age (12–10 Ma) of the Miocene pluton (Fig. 5; Cai et al., 2020; Chen and Chen, 2020). Our new ZHe dates (i.e., samples TK1801, TK1808–TK1814, and TK1816) vary within a relatively narrow range between 9.6 Ma and 8.1 Ma, whereas our new AHe dates vary between 9.6 Ma and 6.0 Ma. The ZHe and AHe dates have no clear relationship with their location along the northern Tashkurgan fault or with elevation (Figs. 5 and S3a). The AHe dates from samples TK1801, TK1808, TK1809, and TK1812–TK1814 vary in the range of 9.6–7.9 Ma and clearly overlap with the ZHe dates within sd, indicating rapid post-emplacement cooling. The remaining three AHe dates (samples TK1810, TK1811, and TK1816) range from 7.5 Ma to 6.0 Ma, which is quite younger than the intrusion age of the pluton. Although sample TK1810 includes only one acceptable single-grain AHe date and sample TK1816 has an over-dispersed AHe date distribution ranging from 10.5 Ma to 4.4 Ma, we tentatively suggest that these AHe dates could record exhumation-related cooling. Overall, most data on the footwall of the northern Tashkurgan fault record rapid cooling related to the intrusion of the Miocene pluton, which is consistent with the shallow emplacement depths of the pluton (Jiang et al., 2012). The available constraints on the exhumation after intrusion consist of the three youngest AHe dates, but these constraints do not warrant estimation of the dip-slip displacement along the fault segment through thermokinematic modeling. Based on the approximate closure temperature of the AHe system (65 ± 5 °C; Reiners and Brandon, 2006) and on the assumption of a constant geothermal gradient in this area (30–50 °C/km; Robinson et al., 2007; Thiede et al., 2013; Chen and Chen, 2020), we estimated that since ~ 7 Ma ago, there has been <2 km of exhumation in the footwall of the northern Tashkurgan fault.

5.2. Cooling dates across the southern Tashkurgan fault

On the hanging wall of the southern Tashkurgan fault, previous ZHe, AFT, and AHe dates (12–10 Ma) from a granitic sample (TX-1) overlap with the intrusion age of the rock (Fig. 5), indicating that this sample was also emplaced at a shallow depth and experienced rapid post-emplacement cooling (Chen and Chen, 2020). On the footwall of the fault segment, previous data (i.e., samples TX-3, TX-6, 1.10.10.10G, 2.10.10.10G, 4.10.10.10G, and 7.10.10.10G) record exhumation from ~ 5 Ma to present with a rate of 0.6–0.9 mm/a (Chen and Chen, 2020). The offset between the hanging wall and footwall cooling dates indicates that the southern Tashkurgan fault initiated between 10 Ma and 5 Ma (Chen and Chen, 2020). Our new ZHe and AHe dates (samples TK1817, TK1843, TK1845, and TK1846) from the footwall of the southern Tashkurgan fault range from 5.0 Ma to 1.2 Ma (Fig. 5), supporting onset of normal slip along the fault segment before 5 Ma. An exception among the samples from the footwall of the southern Tashkurgan fault is sample TK1818 that has a ZHe date of ~ 11.8 Ma and an AHe date of ~ 7.8 Ma.

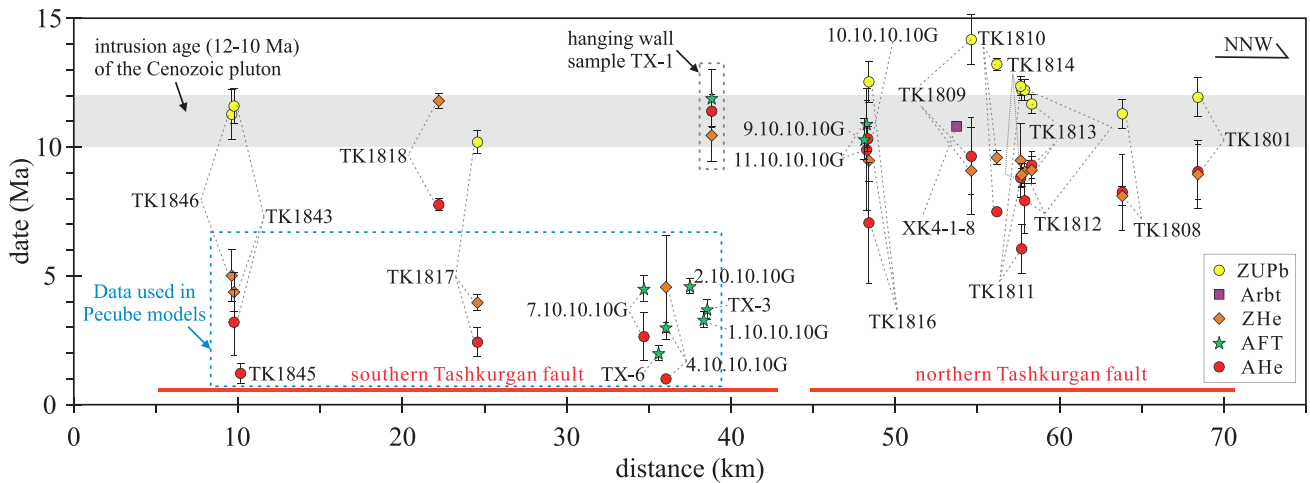


Fig. 5. Cooling dates along the Tashkurgan fault. For swath location, see Fig. 1c. The dates in the swath and from samples TK1809, TK1810, and TK1818 are projected onto the transect. Samples TX-1, TX-3, TX-6, 1.10.10.10G, 2.10.10.10G, 4.10.10.10G, 7.10.10.10G, 9.10.10.10G, 10.10.10.10G, and 11.10.10.10G are from Chen and Chen (2020), sample XK4-1-8 is from Cai et al. (2020), and the samples with “TK18” are from this study. Sample TX-1 is the only hanging wall sample, while the other samples are from the footwalls of the northern and southern segments of the normal fault. The data in the blue dashed box were input into Pecube models. The gray zone shows the intrusion age (12–10 Ma) of the Cenozoic pluton, which is exposed on the footwall of the fault. ZUPb: zircon U-Th-Pb; Arbt: biotite $^{40}\text{Ar}/^{39}\text{Ar}$; ZHe: zircon (U-Th)/He; AFT: apatite fission track; AHe: apatite (U-Th-Sm)/He. (For interpretation of the references to colour in this figure legend, the reader is referred to the web version of this article.)

This sample is from an early Jurassic granitoid, ~11.3 km away from the fault, and ~5 km away from the 12–10 Ma old intrusion (Fig. 1c). The position and dates of this sample indicate that it could have experienced exhumation, which could have occurred at the time of the intrusion of the Miocene pluton, and was likely unaffected by the tectonic activity of the southern Tashkurgan fault.

On the eastern side of the Tashkurgan valley (Fig. 1c), samples TK1824 and TK1828 are located in Permian–Triassic metamorphic rocks and yield ZHe dates of 12–10 Ma, which also record the exhumation that could be associated with the emplacement of the Miocene pluton.

6. Thermokinematic modeling

The thermochronologic data from the footwall of the northern Tashkurgan fault indicate little post-emplacement cooling related to the tectonic activity of the fault segment, whereas the ZHe, AFT, and AHe data (i.e., samples TK1817, TK1843, TK1845, TK1846, TX-3, TX-6, 1.10.10.10G, 2.10.10.10G, 4.10.10.10G, and 7.10.10.10G) from the footwall of the southern Tashkurgan fault record significant exhumation driven by the normal slip along the fault segment. Thus, we focused our modeling on the southern Tashkurgan fault to constrain its slip rate with the aid of a 3-D thermokinematic model for the exhumation of the fault footwall using the Pecube code (version 4.2.1; Braun, 2003; Braun et al., 2012). This model was implemented into an inversion scheme based on the neighborhood algorithm in order to optimize a prediction of the observed thermochronometric dates (Braun et al., 2012). To evaluate the consistency between the predicted and observed dates, a misfit function, ϕ , was used:

$$\phi = \frac{1}{N} \sqrt{\sum_{i=1}^N \left(\frac{A_o_i - A_p_i}{sd_i} \right)^2} \quad (3)$$

where N is the number of thermochronologic dates, A_o is the observed date, A_p is the predicted date, and sd is the one standard deviation of the observed date (Braun et al., 2012).

6.1. Model setup

In this study, we tested three tectono-geomorphic scenarios: (1) constant slip rate on the southern Tashkurgan fault with steady state

topography (model STKF1), (2) constant slip rate on the fault with evolving topography (model STKF2), and (3) two-stage partitioning of slip on the fault with steady state topography (model STKF3). The surface topography in models STKF1 and STKF3 is in steady state and was defined by the present-day topography. In model STKF2, the initial topography was set to a flat surface with an elevation of 3200 m that is the present-day elevation of the hanging wall of the southern Tashkurgan fault, and it evolved linearly towards the modern topography during the simulation.

The initiation age and geometry of the southern Tashkurgan fault are poorly constrained by the available data. To reduce the number of free parameters, we fixed initiation at 6.5 Ma, which is the initiation age of the southern Kongur Shan fault (Chen et al., 2023) and is bracketed by post-emplacement cooling dates and fault exhumation-related dates. We set the southern Tashkurgan fault as a planar feature without curvature (Fig. 6). Based on the dip angles of the triangular facets along the southern Tashkurgan fault (Fig. 2b), the dip of the fault segment was set to 45°. The strike and surface extent of the fault segment were determined by the surface trace of the fault. Our models focus on the footwall exhumation at shallow depths of <10 km; thus, we set the base of the fault segment to a depth of 10 km below sea level. The slip rate on the normal fault was taken as an unknown parameter and was set in a range of 0–5 mm/a.

The model domain has a surface extent of ~30 × 35 km. The base of the thermal model was set to 70 km depth below sea level based on the crust thickness in the study area (Schneider et al., 2019; Xu et al., 2021). The present-day temperatures in the uppermost mantle range from 700 °C to 800 °C (Mechie et al., 2012). Thus, the basal boundary temperature was set in a range of 600–800 °C. At the model surface, temperatures decrease with increasing elevation from 3.6 °C at an elevation of ~3100 m (Weather China, 2020) following an atmospheric lapse rate of 6.5 °C/km (Barry, 2008). Because the footwall of the southern Tashkurgan fault mainly consists of granitoids (Fig. 1c; Jiang et al., 2012; Robinson et al., 2012; Tang et al., 2022), thermal properties, including a high heat production, were selected accordingly. For details on model input parameters, see Table 2.

6.2. Helium diffusion kinetic parameters

To predict dates in our thermokinematic models, we select kinetic

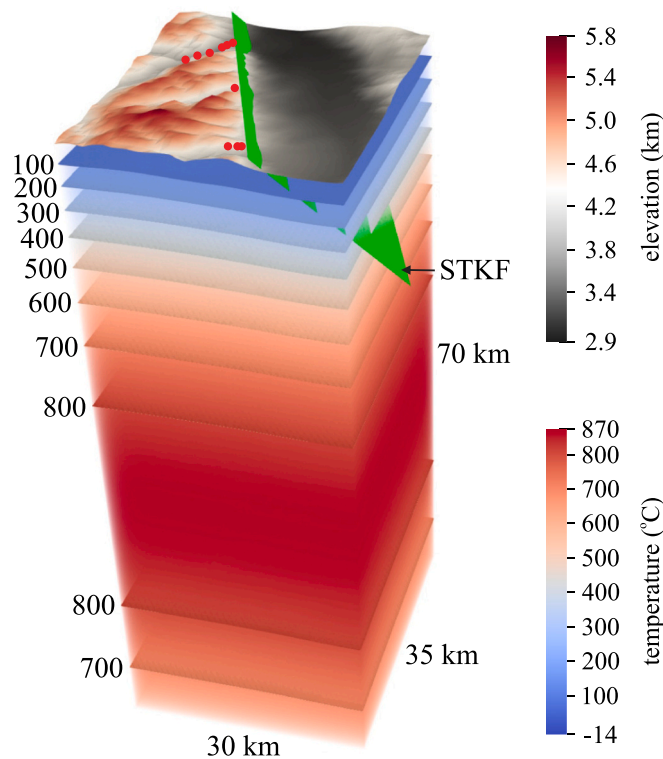


Fig. 6. Thermokinematic model boundary conditions and temperature gradients. The kinematic model shows normal slip along the southern Tashkurgan fault (STKF), which has a dip of 45°. The red dots represent the thermochronologic samples used in Pecube model. The modern topography is derived from the global elevation database GTOPO30. (For interpretation of the references to colour in this figure legend, the reader is referred to the web version of this article.)

Table 2
Model parameters.

Parameter name and unit	Parameter range in inversions	Reference
Crustal density (kg/m ³)	2650	Drury (1987); Schön (2015a)
Thermal diffusivity (km ² /Ma)	31.6	Drury (1987); Eppelbaum et al. (2014)
Heat production (μW/m ³)	2	Hasterok et al. (2018)
Heat capacity (J/kg/K)	1000	Drury (1987); Eppelbaum et al. (2014); Schön (2015b)
Heat production rate (°C/Ma)	23.8	
Mean annual surface temperature in Tashkurgan County (3100 m above sea level) (°C)	3.6	Weather China (2020)
Atmospheric lapse rate (°C/km)	6.5	Barry (2008)
Basal temperature (°C)	600 to 800	Mechie et al. (2012)
Slip rate on the normal fault (mm/a)	0 to 5	
Running time (Ma)	6.5–0	Chen et al. (2023)
Horizontal node spacing (decimal degree)	0.0083333	
Vertical node spacing (km)	1	
Model domain (width × length) (km)	~30 × 35	
Base depth (km)	–70	Schneider et al. (2019); Xu et al. (2021)

parameters which define how helium (He) diffuses in apatite and zircon. Controlling factors for He diffusion include the composition, the size of the diffusion domain (i.e., grain size), and the radiation damage (Reiners and Brandon, 2006; Shuster et al., 2006; Shuster and Farley, 2009;

Gautheron et al., 2009, 2013; Guenther et al., 2013). We cannot account for the effect of composition because we do not have enough compositional data. However, we can account for the size of the diffusion domain and for the radiation damage for individual grains and then average across the grains comprising one sample.

The model input data include only the samples along the southern Tashkurgan fault, and these comprise four samples (TK1817, TK1843, TK1845, and TK1846) from this study and additional samples from Chen and Chen (2020) (Figs. 1c and 5). The apatite samples from this study have AHe dates younger than 5 Ma and low-to-medium eU values of 9–45 ppm (Fig. S1a). The new zircon samples also have ZHe dates younger than 5 Ma but have eU contents up to 4833 ppm (Fig. S1b). Therefore, we did not account for the radiation damage in the apatites but we accounted for the grain size calculating the diffusivity factor (D_0/a^2) for each apatite grain. This was derived using the frequency factor (D_0) value of 2.0×10^{-3} cm²/s (Gautheron et al., 2009) and the equivalent spherical radius ($a = R_s$) of each grain. The D_0/a^2 values of all input apatites range from 138 s⁻¹ to 239 s⁻¹ (Table S1). We set the activation energy (E_a) value to 109.2 kJ/mol, which was given in Gautheron et al. (2009). For the new zircon data, we calculated the D_0/a^2 values taking into account both the effects of grain size and radiation damage by using the empirical relationship between D_0 and alpha dose established by Guenther et al. (2013). The alpha dose reflects the total alpha-decay damage accumulated since the last high-temperature heating event (Guenther et al., 2013). Given that our samples come from a Miocene pluton, we assumed that the modeled zircons have accumulated radiation damage since the emplacement of the intrusion (i.e., 12–10 Ma ago). This assumption is consistent with almost all of the single-grain zircon ²⁰⁶Pb/²³⁸U dates, which vary in the range of 12.7–9.8 Ma (Table S3). Only one zircon (TK1817z2) has a U-Pb date of ~198 Ma, which is much older than the intrusion age of the Miocene pluton. This old date could relate to an inherited zircon and indicates the possibility of complex thermal histories. However, we calculated the alpha dose of this zircon using the average of the other four available zircon U-Pb dates from sample TK1817. The U-Pb dates of the other 14 modeled zircons were used to calculate the alpha dose of each zircon. The effective alpha doses, D_0/a^2 values, and a consistent E_a value of all input zircon grains are 2.9×10^{16} – 1.6×10^{17} α/g, 1.1×10^4 – 1.4×10^5 s⁻¹, and 165 kJ/mol, respectively (Table S2).

The additional samples (TX-3, TX-6, 1.10.10.10G, 2.10.10.10G, 4.10.10.10G, and 7.10.10.10G) from Chen and Chen (2020) contain AHe, ZHe, and AFT dates. For the AHe dates, we also calculated the D_0/a^2 values using the D_0 value of 2.0×10^{-3} cm²/s and set the E_a value to 109.2 kJ/mol (Gautheron et al., 2009). Two AHe samples give mean D_0/a^2 values of 37 s⁻¹ and 68 s⁻¹, respectively. For the ZHe date, we assumed that radiation damage accumulated since 11 Ma, which is taken as the intrusion age. Four zircons from the ZHe sample yield an average effective alpha dose of 3.0×10^{16} α/g, an average D_0/a^2 value of 1.5×10^5 s⁻¹, and a consistent E_a value of 165 kJ/mol. The AFT dates were predicted using the kinetic parameters of Crowley et al. (1991), which are valid for the most common variety of apatite in nature that is fluorapatite.

6.3. Model results

6.3.1. Constant slip rate on the southern Tashkurgan fault with steady state topography (model STKF1)

In inversion model STKF1, the slip rate on the southern Tashkurgan fault was assumed to remain constant with a value of <5 mm/a. The steady state surface topography was defined by the present-day topography. The number of iterations and the number of model runs in each iteration were respectively set to 201 and 8, which correspond to 1608 forward models. The misfit, which reflects the goodness-of-fit between predicted and observed dates (Eq. (3); Braun et al., 2012), has a lowest value of 2.35 in this model.

The only free parameters in this model are the slip rate and the basal temperature, and their values for the lowest-misfit solution can be found

in Table 3 and Fig. 7a: (1) the slip rate on the southern Tashkurgan fault is defined at values of between 1.3 mm/a and 1.6 mm/a, with a best-fit value of ~ 1.4 mm/a; and (2) the temperature at the base of the model is constrained at a best-fit value of 659 °C. The predicted ZHe dates obtained from a forward model using the preferred parameters match well with the observed dates, while most of the predicted AFT and AHe dates have larger deviations from their corresponding observed dates (Fig. 8a).

6.3.2. Constant slip rate on the southern Tashkurgan fault with evolving topography (model STKF2)

In this inversion model, the slip rate on the southern Tashkurgan fault was again assumed to remain constant with a value of <5 mm/a. In order to quantify the impact of growing topography on the slip rate and on the footwall thermochronologic data, the topography in this model evolved linearly from a flat surface with an elevation of 3200 m towards the modern topography over the last 6.5 Ma. This inversion set also comprises 1608 forward models and gives a lowest misfit value of 2.44.

The two estimated parameter values for the lowest-misfit solution can be found in Table 3 and Fig. 7b: (1) the slip rate on the southern Tashkurgan fault is defined at values of between 1.4 mm/a and 1.6 mm/a, with a best-fit value of ~ 1.5 mm/a; and (2) the basal temperature is constrained at a best-fit value of 612 °C. The best predicted ZHe dates from this inversion model also match well with the observed dates, but most of the predicted AFT and AHe dates have larger deviations from the observed dates (Fig. 8b).

6.3.3. Two-stage partitioning of slip on the southern Tashkurgan fault with steady state topography (model STKF3)

To investigate the potential for temporal variation in the slip rate on the southern Tashkurgan fault over the last 6.5 Ma, a change in slip rate was assumed to have occurred at a transition time between 5 Ma and 2 Ma. Both the slip rate at the first phase (slip rate 1) and the rate at the second phase (slip rate 2) were taken as unknowns with a range from 0 mm/a to 5 mm/a. The steady state topography was defined by the modern topography. This inversion set contains 1608 forward models and yields a lowest misfit value of 2.35.

The four free parameter values for the lowest-misfit solution can be found in Table 3 and Fig. 7c, d: (1) the best estimate for a change in slip rate is 4.5 Ma; (2 and 3) the slip rate 1 is defined at a best-fit value of ~ 1.6 mm/a, while the slip rate 2 is defined at values of between 1.2 mm/a and 1.5 mm/a, with a best-fit value of ~ 1.4 mm/a; and (4) the basal temperature in this model is defined at a best-fit value of 723 °C. Similar to models STKF1 and STKF2, the predicted ZHe dates from this model match well with the observed dates, while most of the predicted AFT and AHe dates deviate from the observed dates (Fig. 8c).

7. Discussion

7.1. Extension and exhumation along the southern Tashkurgan fault

As the sole boundary fault of the Tashkurgan valley (Fig. 1c), the southern Tashkurgan fault controls the \sim E–W extension along the

valley. The initiation age of the southern Tashkurgan fault is poorly constrained between 10 Ma and 5 Ma (Chen and Chen, 2020; this study). In the tested scenarios, the initiation age could affect the resulting slip rate on the fault segment, especially for the slip rate before 5 Ma that is not constrained by the footwall thermochronologic dates. We assumed that the initiation age of the southern Tashkurgan fault is consistent with the onset timing (i.e., 6.5 Ma) of normal slip along the southern Kongur Shan fault, which is another significant fault in the southern portion of the Kongur Shan extensional system (Robinson et al., 2007; Cao et al., 2013a; Thiede et al., 2013; Chen et al., 2023). Another limitation of the tested scenarios comes from the assumption of a specific geometry for the southern Tashkurgan fault and in particular of a dip angle of 45°. This value is inferred from field observations that constrain the minimum dip angle of the fault (Fig. 2b). However, it is possible that the true dip of the fault at shallow crustal levels is $>45^\circ$, but we have no other observations to better constrain the dip angle.

In this study, all the tested scenarios for the southern Tashkurgan fault reproduce quite well the four available ZHe dates, two out of six AFT dates, but rather poorly some of the AFT and AHe dates (Fig. 8a, b, c). Both the AFT and AHe dates are very scattered and do not show clear correlation in space or in elevation (Figs. 5 and S3b); thus, most likely no model could easily reproduce these data. We speculate that the date scatter may reflect variable track annealing and He-diffusion properties of the dated apatites, which our model does not account for because we assumed constant kinetic parameters for the date prediction.

We ran two tectonomorphic scenarios (models STKF1 and STKF2) for uplift of the footwall of the southern Tashkurgan fault to evaluate the impact of topographic changes on the thermochronologic data from the footwall and on the slip rate on the fault segment. The surface topography in model STKF1 does not change and is defined by the modern topography, while the topography in model STKF2 evolves linearly from a flat surface with an elevation of 3200 m to the modern topography over the last 6.5 Ma. The modeling results show that there is only a small difference between the lowest misfit value in model STKF1 (2.35) and the value in model STKF2 (2.44) and these two models yield similar best-fit predicted dates (Fig. 8a, b), indicating that our model cannot resolve how the topographic changes may have impacted the distribution of cooling dates. It is most likely because the modeling thermochronologic samples were collected along the river valleys and the maximum elevation difference among the samples is ~ 425 m (Figs. 1c and S3b; Table S4), which is much less than the modern maximum difference of ~ 2300 m across the southern Tashkurgan fault (Fig. 2b). In other words, the samples may not be distributed spatially enough to capture the effect of topography. The slip rates on the southern Tashkurgan fault are also similar for models STKF1 (1.4 mm/a) and STKF2 (1.5 mm/a) (Fig. 7a, b).

Inversion model STKF3 was constructed to test for a possible change of slip rate on the southern Tashkurgan fault, and it yields a best-fit slip rate of 1.6 mm/a for the time interval 6.5–4.5 Ma and another rate of 1.4 mm/a for the time interval 4.5–0 Ma (Fig. 7d). These two slip rates are similar and give an average rate of ~ 1.5 mm/a, which is close to the slip rates from models STKF1 and STKF2. The lowest misfit value in model STKF3 (2.35) is equal to that in model STKF1, indicating that our model cannot resolve how the change of slip rate may have impacted the date distribution. Thus, we suggest that the southern Tashkurgan fault probably has had a constant slip rate of 1.4–1.5 mm/a. Based on the dip of the fault in our models, the resulting constant slip rate corresponds to 6–7 km of both horizontal extension and footwall uplift with a rate of ~ 1.0 mm/a since 6.5 Ma ago.

In addition, the basal temperature in each tested scenario was not constrained well, and the resulting best-fit temperature values vary from 612 °C to 723 °C (Fig. 7a, b, c). However, the three models give similar slip rates on the southern Tashkurgan fault. We believe that the basal temperature has insignificant effect on the slip rate, which is because of the deep depth of the model base (70 km depth below sea level) and the shallow crustal levels (<10 km) that were involved into exhumation.

Table 3
Inversion results.

Parameter name and unit	model STKF1	model STKF2	model STKF3
Number of simulations	1608	1608	1608
Best misfit	2.35	2.44	2.35
Basal temperature (°C)	659 (600 to 800)	612 (600 to 800)	723 (600 to 800)
Time step	1	1	2
Transition time (Ma)	n/a	n/a	4.5 (5 to 2)
Slip rate 1 (mm/a)	1.4 (0 to 5)	1.5 (0 to 5)	1.6 (0 to 5)
Slip rate 2 (mm/a)	n/a	n/a	1.4 (0 to 5)

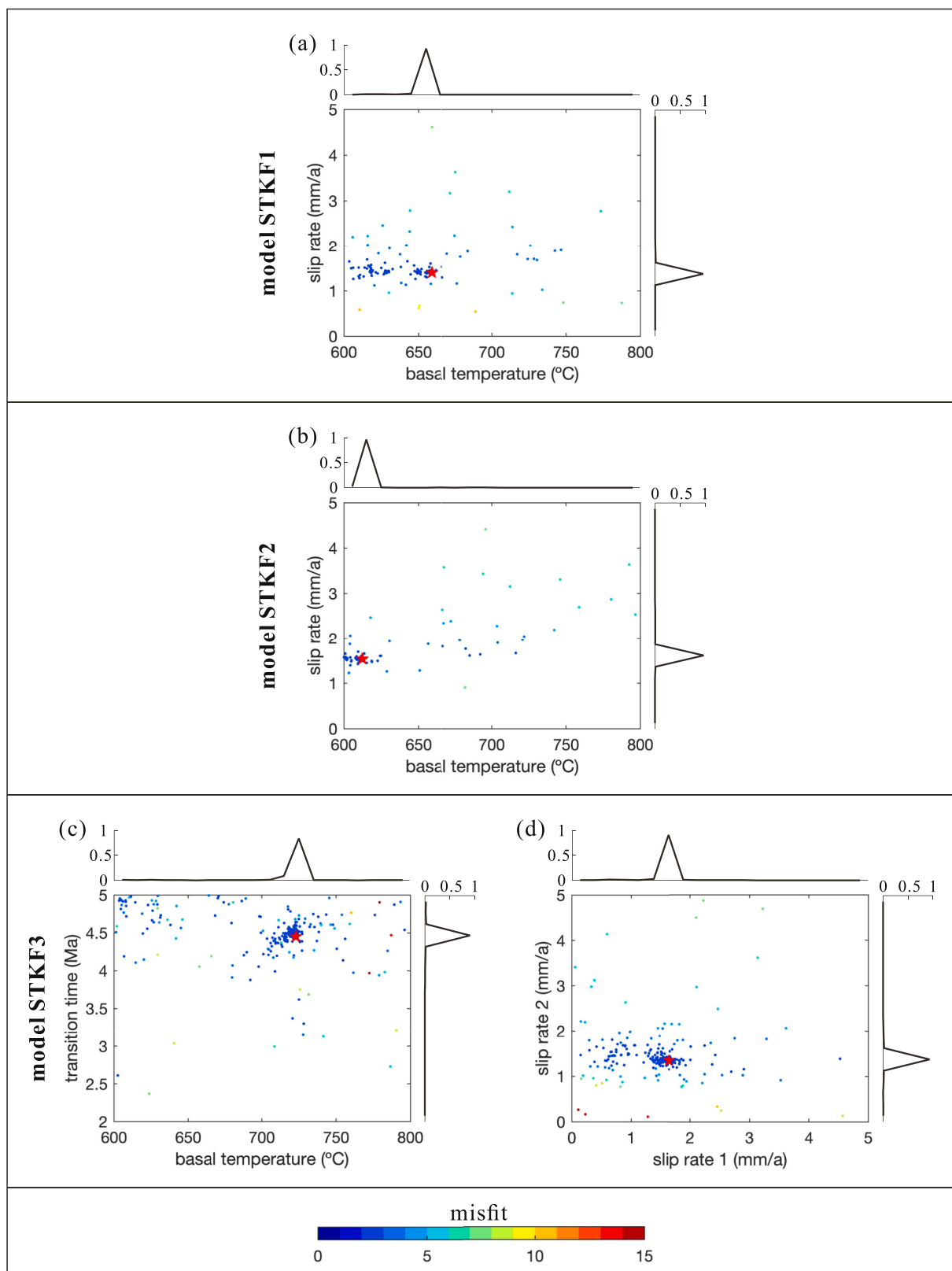


Fig. 7. Inversion results for models (a) STKF1, (b) STKF2, and (c) and (d) STKF3. Each dot represents a single forward model, and its colour corresponds to the misfit of the forward model. The red star represents the parameter combination obtained from the forward model with the lowest misfit. Probability density functions (PDFs) are shown for each parameter. (For interpretation of the references to colour in this figure legend, the reader is referred to the web version of this article.)

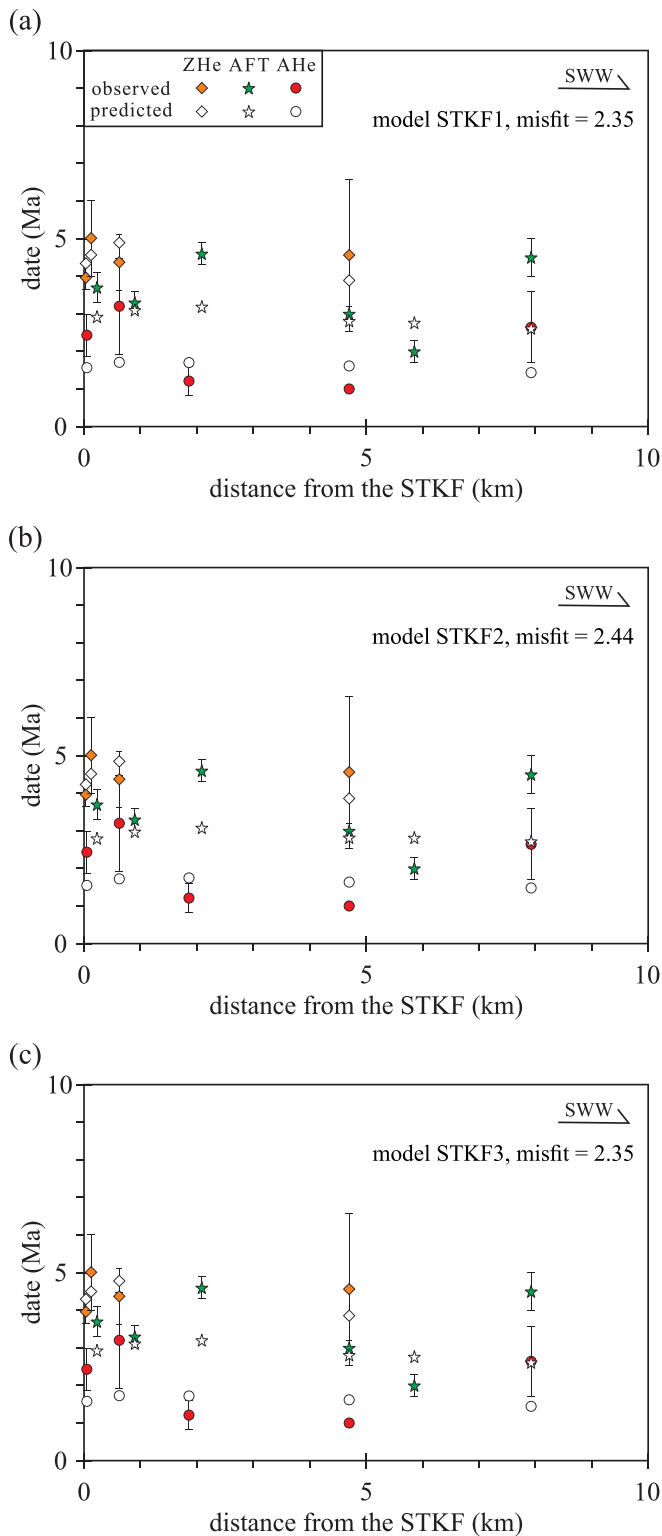


Fig. 8. Observed-versus-predicted cooling dates from the forward model with the lowest misfit in models (a) STKF1, (b) STKF2, and (c) STKF3. ZHe: zircon (U-Th)/He; AFT: apatite fission track; AHe: apatite (U-Th-Sm)/He.

The highest temperatures were found at the depths of 40–50 km rather than at the model base (Fig. 6), which also implies that the basal temperature could have no impact on the geothermal gradients at shallow depths and further on the slip rate of the fault segment.

7.2. Segmentation of the Tashkurgan fault

The Tashkurgan normal fault can be divided into a northern segment and a southern one (Fig. 1c). The elevation difference across the northern Tashkurgan fault (~500 m) is significantly less than the difference across the southern Tashkurgan fault (~2300 m), and triangular facets are observed only along the southern segment (Fig. 2a, b). Further, both the local relief and the normalized channel steepness index (k_{sn}) values in the mountain front along the northern Tashkurgan fault (i.e., within ~5 km from the fault) are generally less than those in the front along the southern fault segment (Fig. 3a, b). The χ -elevation profiles for the trunk channels in the drainage basins (i.e., 1–4) from the footwall of the northern fault segment are much closer to straight lines than the profiles for the trunk channels in the basins (i.e., 5–8) from the footwall of the southern fault segment (Fig. 4). Along the trunk channel of drainage basin 5, the uppermost knickpoint could be associated with lithologic changes because it is located at the boundary between granitoids and sedimentary/metamorphic rocks, while the lower two knickpoints may be tectonic in origin since they lie within granitic rocks and are close to the southern Tashkurgan fault (Figs. 3b and 4). These geomorphic features indicate that the southern Tashkurgan fault is more active than the northern segment, which is also supported by the ^{10}Be -derived basin-wide erosion rates (Wu et al., 2023). Moreover, almost all of the upstream channels in drainage basin 5 have k_{sn} values of <100 (Fig. 3b), and the upper reach of trunk channel 5 generally has a lower slope than its lower reach on the χ -elevation plot (Fig. 4), indicating that the activity of the southern Tashkurgan fault is limited spatially to the region within ~10 km from the fault. This is consistent with the relatively old ZHe (~11.8 Ma) and AHe (~7.8 Ma) dates from sample TK1818 that is ~11.3 km away from the fault segment and records little post-6.5 Ma exhumation.

The northern Tashkurgan fault has low magnitude of dip-slip displacement as indicated by the little exhumation (<2 km) recorded since ~7 Ma ago by the thermochronologic data from its footwall (Fig. 5). However, the low-temperature thermochronologic dates from the footwall of the southern Tashkurgan fault excepting the dates from sample TK1818 range from 5 Ma to 1 Ma, considerably younger than the dates to the north (Fig. 5). These dates combined with 3-D thermokinematic modeling allow us to make a conclusion that the southern Tashkurgan fault has accommodated 6–7 km of both horizontal extension and footwall uplift since 6.5 Ma ago. Thus, the southern Tashkurgan fault is responsible for the ~E–W extension along the southernmost portion of the Kongur Shan extensional system, while the northern Tashkurgan fault plays only a minor role in the extension.

7.3. Fault-slip transfer in the southern Kongur Shan extensional system

Normal faulting from the late Miocene to the present along the southern portion of the Kongur Shan extensional system has resulted in exhumation of the western margin of the Muztaghata dome and of the Miocene pluton that is located on the footwall of the Tashkurgan fault (Fig. 1c) (Robinson et al., 2007; Cao et al., 2013a; Thiede et al., 2013; Chen and Chen, 2020; Chen et al., 2023). The southern Kongur Shan fault initiated at ~6.5 Ma and has an extension magnitude of 8–9 km, whereas the Tahman transfer fault has a low magnitude of dip-slip displacement (Chen et al., 2023). In this study, the exhumation magnitude of the footwall of the northern Tashkurgan fault was estimated to be <2 km. The onset timing of normal slip along the southern Tashkurgan fault is still poorly constrained and could be the same time as the southern Kongur Shan fault. Our new modeling results indicate that the southern Tashkurgan fault has accommodated 6–7 km of horizontal extension since ~6.5 Ma. Thus, the ~E–W extension along the Tahman and Tashkurgan valleys is controlled by the normal slip along the southern Kongur Shan and southern Tashkurgan faults, respectively, while the other faults, including the transfer fault, have minor effects on the extension (Fig. 9). In other words, the extension at any site along the southern Kongur Shan extensional system can be primarily attributed to

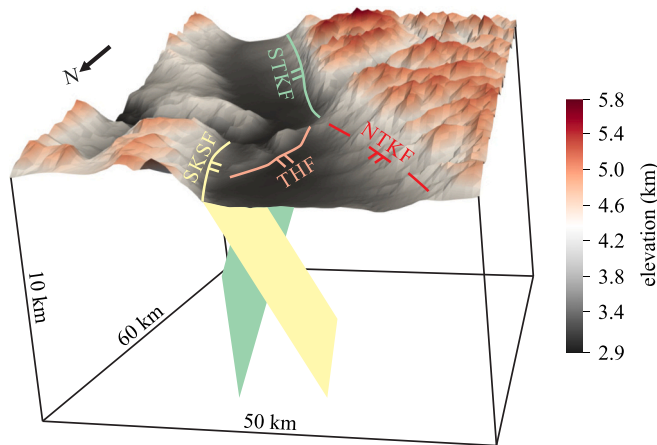


Fig. 9. Modern topography and normal faults along the southern portion of the Kongur Shan extensional system. NTKF: northern Tashkurgan fault; SKSF: southern Kongur Shan fault; STKF: southern Tashkurgan fault; THF: Tahman fault.

normal faulting along a single border fault. A similar structural style is common in several regions of extensional tectonics (Gawthorpe and Hurst, 1993). As a rare example in neotectonic settings, the southern Kongur Shan extensional system could be helpful to study the structural characteristics of an interbasin transfer zone with a transfer fault.

8. Conclusions

In this study, we carried out geomorphologic analysis to evaluate the relative tectonic activity along the Tashkurgan fault. Our new AHe and ZHe data, in conjunction with previously published work on the Tashkurgan fault, allow us to constrain the late Miocene to present extension and exhumation along different segments of the fault. Our main findings are:

- (1) Geomorphic features, including local relief, normalized channel steepness index (k_{sn}), and river χ -plots, indicate that the southern Tashkurgan fault is more active than the northern Tashkurgan fault.
- (2) The footwall thermochronologic dates show that the southern Tashkurgan fault is responsible for the ~E–W extension along the southernmost portion of the Kongur Shan extensional system, while the northern Tashkurgan fault plays a minor role in the extension.
- (3) The onset timing of the Tashkurgan fault is poorly constrained at 10–5 Ma, but we infer that the southern fault segment initiated at ~6.5 Ma, which is the initiation age of the southern Kongur Shan fault.
- (4) The thermokinematic modeling results show that the southern Tashkurgan fault probably has had a constant slip rate of 1.4–1.5 mm/a, which corresponds to 6–7 km of both horizontal extension and footwall uplift.
- (5) The extension at any site along the southern Kongur Shan extensional system can be primarily attributed to normal faulting along a single border fault, which is a typical characteristic of an interbasin transfer zone with a transfer fault.

Supplementary data to this article can be found online at <https://doi.org/10.1016/j.tecto.2024.230305>.

CRedit authorship contribution statement

Shenqiang Chen: Writing – review & editing, Writing – original draft, Visualization, Software, Methodology, Investigation, Conceptualization. **Maria Giuditta Fellin:** Writing – review & editing, Supervision, Methodology. **Sean D. Willett:** Writing – review & editing, Supervision, Methodology. **Colin Maden:** Methodology. **Marcel Guillong:** Methodology. **Hanlin Chen:** Investigation. **Yaguang Chen:** Investigation. **Rong Yang:** Investigation.

Declaration of competing interest

The authors declare that they have no known competing financial interests or personal relationships that could have appeared to influence the work reported in this paper.

Data availability

Data will be made available on request.

Acknowledgments

We thank editor Samuel Angiboust and reviewers Edward Sobel and Pierre Valla for their constructive comments. This study was funded by the National Natural Science Foundation of China (41720104003 and 41972214). S. Chen received a PhD grant (201706320352) from the China Scholarship Council and a postdoc grant (GZC20232488) from the China Postdoc Council.

References

- Angiolini, L., Zanchi, A., Zanchetta, S., Nicora, A., Vezzoli, G., 2013. The Cimmerian geopuzzle: new data from South Pamir. *Terra Nova* 25, 352–360. <https://doi.org/10.1111/ter.12042>.
- Barry, R.G., 2008. *Mountain Weather and Climate*, third ed. Cambridge University Press, Cambridge. <https://doi.org/10.1017/CBO9780511754753>.
- Bian, S., Gong, J., Zuza, A.V., Yang, R., Tian, Y., Ji, J., Chen, H., Xu, Q., Chen, L., Lin, X., Cheng, X., Tu, J., Yu, X., 2020. Late Pliocene onset of the Cona rift, eastern Himalaya, confirms eastward propagation of extension in Himalayan–Tibetan orogen. *Earth Planet. Sci. Lett.* 544, 116383 <https://doi.org/10.1016/j.epsl.2020.116383>.
- Boehne, P., Harrison, T.M., 2014. A meta-analysis of geochronologically relevant half-lives: what's the best decay constant? *Int. Geol. Rev.* 56, 905–914. <https://doi.org/10.1080/00206814.2014.908420>.
- Braun, J., 2003. Pecube: a new finite-element code to solve the 3D heat transport equation including the effects of a time-varying, finite amplitude surface topography. *Comput. Geosci.* 29, 787–794. [https://doi.org/10.1016/S0098-3004\(03\)00052-9](https://doi.org/10.1016/S0098-3004(03)00052-9).
- Braun, J., van der Beek, P., Valla, P., Robert, X., Herman, F., Glotzbach, C., Pedersen, V., Perry, C., Simon-Labric, T., Prigent, C., 2012. Quantifying rates of landscape evolution and tectonic processes by thermochronology and numerical modeling of crustal heat transport using PECUBE. *Tectonophysics* 524–525, 1–28. <https://doi.org/10.1016/j.tecto.2011.12.035>.
- Burbank, D.W., Anderson, R.S., 2012. *Tectonic Geomorphology*, second ed. John Wiley & Sons. <https://doi.org/10.1002/97811444345063>.
- Burtman, V.S., 2010. Tien Shan, Pamir, and Tibet: history and geodynamics of Phanerozoic oceanic basins. *Geotectonics* 44, 388–404. <https://doi.org/10.1134/S001685211005002X>.
- Burtman, V.S., Molnar, P., 1993. Geological and geophysical evidence for deep subduction of continental crust beneath the Pamir. *Spec. Paper Geol. Soc. Am.* 281, 1–76. <https://doi.org/10.1130/SPE281-p1>.
- Cai, Z., Xu, Z., Cao, H., Robinson, A.C., Li, G., Xu, X., 2017. Miocene exhumation of northeast Pamir: Deformation and geo/thermochronological evidence from western Muztaghata shear zone and Kuke ductile shear zone. *J. Struct. Geol.* 102, 130–146. <https://doi.org/10.1016/j.jsg.2017.07.010>.
- Cai, Z., He, B., Liu, R., 2020. Emplacement of granitic pluton and Cenozoic deformation in the Wenquan region, Tashkurgan, Xinjiang: the implications for the Miocene tectonic evolution of the Northeast Pamir. *Ac. Petrol. Sin.* 36, 3137–3151 (in Chinese with English abstract). [10.18654/1000-0569/2020.10.12](https://doi.org/10.18654/1000-0569/2020.10.12).
- Cai, Z., He, B., Li, G., Jiao, C., Yun, X., 2021. Early Cretaceous deformation in the southern Tashkurgan region: Implications for the tectonic evolution of the northeastern Pamir. *China Geol.* 1, 67–76. <https://doi.org/10.31035/cg2021023>.
- Cao, K., Wang, G., van der Beek, P., Bernert, M., Zhang, K., 2013a. Cenozoic thermotectonic evolution of the northeastern Pamir revealed by zircon and apatite fission-track thermochronology. *Tectonophysics* 589, 17–32. <https://doi.org/10.1016/j.tecto.2012.12.038>.
- Cao, K., Bernert, M., Wang, G., van der Beek, P., Wang, A., Zhang, K., Enkelmann, E., 2013b. Focused Pliocene–Quaternary exhumation of the Eastern Pamir domes, western China. *Earth Planet. Sci. Lett.* 363, 16–26. <https://doi.org/10.1016/j.epsl.2012.12.023>.
- Chen, S., Chen, H., 2020. Late Cenozoic activity of the Tashkurgan normal fault and implications for the origin of the Kongur Shan extensional system, eastern Pamir. *J. Earth Sci.* 31, 723–734. <https://doi.org/10.1007/s12583-020-1282-1>.
- Chen, S., Chen, H., Zhu, K., Tao, Y., 2021. Petrogenesis of the Middle–Late Triassic S- and I-type granitoids in the eastern Pamir and implications for the Tanyamas–Jinshajiang Paleo-Tethys Ocean. *Int. J. Earth Sci.* 110, 1213–1232. <https://doi.org/10.1007/s00531-021-02013-z>.
- Chen, S., Fellin, M.G., Willett, S.D., Maden, C., Guillong, M., Chen, H., Chen, Y., 2023. Late Miocene to present synchronous extension and contraction in the eastern Pamir:

- Insights from inversion of thermochronologic data across the southern Muztaghata dome. *Geol. Soc. Am. Bull.* <https://doi.org/10.1130/B36953.1>.
- Cowgill, E., 2010. Cenozoic right-slip faulting along the eastern margin of the Pamir salient, northwestern China. *Geol. Soc. Am. Bull.* 122, 145–161. <https://doi.org/10.1130/B26520.1>.
- Crowley, K.D., Cameron, M., Schaefer, R.L., 1991. Experimental studies of annealing of etched fission tracks in fluorapatite. *Geochim. Cosmochim. Ac.* 55, 1449–1465. [https://doi.org/10.1016/0016-7037\(91\)90320-5](https://doi.org/10.1016/0016-7037(91)90320-5).
- Drury, M.J., 1987. Thermal diffusivity of some crystalline rocks. *Geothermics* 16, 105–115. [https://doi.org/10.1016/0375-6505\(87\)90059-9](https://doi.org/10.1016/0375-6505(87)90059-9).
- Eppelbaum, L., Kutasov, I., Pilchin, A., 2014. Thermal properties of rocks and density of fluids. In: *Applied Geothermics*. Springer, Berlin, Heidelberg. https://doi.org/10.1007/978-3-642-34023-9_2.
- Gautheron, C., Tassan-Got, L., Barbarand, J., Pagel, M., 2009. Effect of alpha-damage annealing on apatite (U-Th)/He thermochronology. *Chem. Geol.* 266, 157–170. <https://doi.org/10.1016/j.chemgeo.2009.06.001>.
- Gautheron, C., Barbarand, J., Ketcham, R.A., Tassan-Got, L., van der Beek, P., Pagel, M., Pinna-Jamme, R., Couffignal, F., Fialin, M., 2013. Chemical influence on α -recoil damage annealing in apatite: Implications for (U-Th)/He dating. *Chem. Geol.* 351, 257–267. <https://doi.org/10.1016/j.chemgeo.2013.05.027>.
- Gawthorpe, R.L., Hurst, J.M., 1993. Transfer zones in extensional basins: their structural style and influence on drainage development and stratigraphy. *J. Geol. Soc. Lond.* 150, 1137–1152. <https://doi.org/10.1144/gsjgs.150.6.1137>.
- Guenther, W.R., Reiners, P.W., Ketcham, R.A., Nasdala, L., Giester, G., 2013. Helium diffusion in natural zircon: Radiation damage, anisotropy, and the interpretation of zircon (U-Th)/He thermochronology. *Am. J. Sci.* 313, 145–198. <https://doi.org/10.2475/03.2013.01>.
- Hasterok, D., Gard, M., Webb, J., 2018. On the radiogenic heat production of metamorphic, igneous, and sedimentary rocks. *Geosci. Front.* 9, 1777–1794. <https://doi.org/10.1016/j.gsf.2017.10.012>.
- Hidaka, H., Shimizu, H., Adachi, M., 2002. U-Pb geochronology and REE geochemistry of zircons from Palaeoproterozoic paragneiss clasts in the Mesozoic Kamiaso conglomerate, central Japan: evidence for an Archean provenance. *Chem. Geol.* 187, 279–293. [https://doi.org/10.1016/S0009-2541\(02\)00058-X](https://doi.org/10.1016/S0009-2541(02)00058-X).
- Hourigan, J.K., Reiners, P.W., Brandon, M.T., 2005. U-Th zonation-dependent alpha-ejection in (U-Th)/He chronometry. *Geochim. Cosmochim. Ac.* 69, 3349–3365. <https://doi.org/10.1016/j.gca.2005.01.024>.
- Imrecke, D.B., Robinson, A.C., Owen, L.A., Chen, J., Schoenbohm, L.M., Hedrick, K.A., Lapen, T.J., Li, W., Yuan, Z., 2019. Mesozoic evolution of the eastern Pamir. *Lithosphere* 11, 560–580. <https://doi.org/10.1130/L1017.1>.
- Jiang, Y., Liu, Z., Jia, R., Liao, S., Zhou, Q., Zhao, P., 2012. Miocene potassic granite-syenite association in western Tibetan Plateau: Implications for shoshonitic and high Ba-Sr granite genesis. *Lithos* 134–135, 146–162. <https://doi.org/10.1016/j.lithos.2011.12.012>.
- Ketcham, R.A., Gautheron, C., Tassan-Got, L., 2011. Accounting for long alpha-particle stopping distances in (U-Th-Sm)/He geochronology: Refinement of the baseline case. *Geochim. Cosmochim. Ac.* 75, 7779–7791. <https://doi.org/10.1016/j.gca.2011.10.011>.
- Kirby, E., Whipple, K.X., 2012. Expression of active tectonics in erosional landscapes. *J. Struct. Geol.* 44, 54–75. <https://doi.org/10.1016/j.jsg.2012.07.009>.
- Li, Y., Robinson, A.C., Lapen, T.J., Righter, M., Stevens, M.K., 2020. Muztaghata dome Miocene eclogite facies metamorphism: a record of lower crustal evolution of the NE Pamir. *Tectonics* 38. <https://doi.org/10.1029/2019TC005917> e2019TC005917.
- Li, Y., Robinson, A.C., Zucali, M., Gadoev, M., Oimuhammadzoda, I., Lapen, T.J., Carrapa, B., 2022. Mesozoic tectonic evolution in the Kurgovat-Vanch complex, NW Pamir. *Tectonics* 41. <https://doi.org/10.1029/2021TC007180> e2021TC007180.
- McDowell, F.W., McIntosh, W.C., Farley, K.A., 2005. A precise ^{40}Ar - ^{39}Ar reference age for the Durango apatite (U-Th)/He and fission-track dating standard. *Chem. Geol.* 214, 249–263. <https://doi.org/10.1016/j.chemgeo.2004.10.002>.
- Mechie, J., Yuan, X., Schurr, B., Schneider, F., Sippl, C., Ratschbacher, L., Minaev, V., Gadoev, M., Oimahmadov, I., Abdybaev, U., Moldobekov, B., Orunbaev, S., Negmatullaev, S., 2012. Crustal and uppermost mantle velocity structure along a profile across the Pamir and southern Tien Shan as derived from project TIPAGE wide-angle seismic data. *Geophys. J. Int.* 188, 385–407. <https://doi.org/10.1111/j.1365-246X.2011.05278.x>.
- Mitsuishi, M., Wallis, S.R., Aoya, M., Lee, J., Wang, Y., 2012. E–W extension at 19 Ma in the Kung Co area, S. Tibet: Evidence for contemporaneous E–W and N–S extension in the Himalayan orogen. *Earth Planet. Sci. Lett.* 325–326, 10–20. <https://doi.org/10.1016/j.epsl.2011.11.013>.
- Owen, L.A., Chen, J., Hedrick, K.A., Caffee, M.W., Robinson, A.C., Schoenbohm, L.M., Yuan, Z., Li, W., Imrecke, D.B., Liu, J., 2012. Quaternary glaciation of the Tashkurgan Valley, Southeast Pamir. *Quat. Sci. Rev.* 47, 56–72. <https://doi.org/10.1016/j.quascirev.2012.04.027>.
- Perron, J.T., Royden, L., 2013. An integral approach to bedrock river profile analysis. *Earth Surf. Process. Landf.* 38, 570–576. <https://doi.org/10.1002/esp.3302>.
- Reiners, P.W., Brandon, M.T., 2006. Using thermochronology to understand orogenic erosion. *Annu. Rev. Earth Planet. Sci.* 34, 419–466. <https://doi.org/10.1146/annurev.earth.34.031405.125202>.
- Rembe, J., Sobel, E.R., Kley, J., Terbishaliev, B., Musiol, A., Chen, J., Zhou, R., 2022. Geochronology, geochemistry, and geodynamic implications of Permo-Triassic back-arc basin successions in the North Pamir, Central Asia. *Lithosphere* 2022, 7514691. <https://doi.org/10.2113/2022/7514691>.
- Robinson, A.C., 2015. Mesozoic tectonics of the Gondwanan terranes of the Pamir plateau. *J. Asian Earth Sci.* 102, 170–179. <https://doi.org/10.1016/j.jseas.2014.09.012>.
- Robinson, A.C., Yin, A., Manning, C.E., Harrison, T.M., Zhang, S., Wang, X., 2004. Tectonic evolution of the northeastern Pamir: Constraints from the northern portion of the Cenozoic Kongur Shan extensional system, western China. *Geol. Soc. Am. Bull.* 116, 953–973. <https://doi.org/10.1130/B25375.1>.
- Robinson, A.C., Yin, A., Manning, C.E., Harrison, T.M., Zhang, S., Wang, X., 2007. Cenozoic evolution of the eastern Pamir: Implications for strain-accommodation mechanisms at the western end of the Himalayan-Tibetan orogen. *Geol. Soc. Am. Bull.* 119, 882–896. <https://doi.org/10.1130/B25981.1>.
- Robinson, A.C., Ducea, M., Lapen, T.J., 2012. Detrital zircon and isotopic constraints on the crustal architecture and tectonic evolution of the northeastern Pamir. *Tectonics* 31, TC2016. <https://doi.org/10.1029/2011tc003013>.
- Rutte, D., Ratschbacher, L., Schneider, S., Stübner, K., Stearns, M.A., Gulzar, M.A., Hacker, B.R., 2017a. Building the Pamir-Tibetan Plateau—Crustal stacking, extensional collapse, and lateral extrusion in the Central Pamir: 1. Geometry and kinematics. *Tectonics* 36. <https://doi.org/10.1002/2016TC004293>.
- Rutte, D., Ratschbacher, L., Khan, J., Stübner, K., Hacker, B.R., Stearns, M.A., Enkelmann, E., Jonckheere, R., Pfänder, J.A., Sperner, B., Tichomirowa, M., 2017b. Building the Pamir-Tibetan Plateau—Crustal stacking, extensional collapse, and lateral extrusion in the Central Pamir: 2. Timing and rates. *Tectonics* 36. <https://doi.org/10.1002/2016TC004294>.
- Schmidt, J., Hacker, B.R., Ratschbacher, L., Stübner, K., Stearns, M., Kylander-Clark, A., Cottle, J.M., Alexander, A., Webb, G., Gehrels, G., Minaev, V., 2011. Cenozoic deep crust in the Pamir. *Earth Planet. Sci. Lett.* 312, 411–421. <https://doi.org/10.1016/j.epsl.2011.10.034>.
- Schneider, F.M., Yuan, X., Schurr, B., Mechie, J., Sippl, C., Kufner, S.K., Ratschbacher, L., Tilmann, F., Oimahmadov, I., Gadoev, M., Minaev, V., Abdybaev, U., Orunbaev, S., Ischuk, A., Murodkulov, S., 2019. The crust in the Pamir: insights from receiver functions. *J. Geophys. Res. Solid Earth* 124, 9313–9331. <https://doi.org/10.1029/2019JB017765>.
- Schön, J.H., 2015a. Density, in: Physical properties of rocks. *Dev. Pet. Sci.* 65, 109–118. <https://doi.org/10.1016/B978-0-08-100404-3.00004-4>.
- Schön, J.H., 2015b. Thermal properties, in: Physical properties of rocks. *Dev. Pet. Sci.* 65, 369–414. <https://doi.org/10.1016/B978-0-08-100404-3.00009-3>.
- Schwanghart, W., Kuhn, N.J., 2010. TopoToolbox: a set of Matlab functions for topographic analysis. *Environ. Model. Softw.* 25, 770–781. <https://doi.org/10.1016/j.envsoft.2009.12.002>.
- Schwanghart, W., Scherler, D., 2014. Short Communication: TopoToolbox 2 – Matlab-based software for topographic analysis and modeling in Earth surface sciences. *Earth Surf. Dynam.* 2, 1–7. <https://doi.org/10.5194/esurf-2-1-2014>.
- Shuster, D.L., Farley, K.A., 2009. The influence of artificial radiation damage and thermal annealing on helium diffusion kinetics in apatite. *Geochim. Cosmochim. Ac.* 73, 183–196. <https://doi.org/10.1016/j.gca.2008.10.013>.
- Shuster, D.L., Flowers, R.M., Farley, K.A., 2006. The influence of natural radiation damage on helium diffusion kinetics in apatite. *Earth Planet. Sci. Lett.* 249, 148–161. <https://doi.org/10.1016/j.epsl.2006.07.028>.
- Snyder, N.P., Whipple, K.X., Tucker, G.E., Merritts, D.J., 2000. Landscape response to tectonic forcing: Digital elevation model analysis of stream profiles in the Mendocino triple junction region, northern California. *Geol. Soc. Am. Bull.* 112, 1250–1263. [https://doi.org/10.1130/0016-7606\(2000\)112<1250:LRTTFD>2.0.CO;2](https://doi.org/10.1130/0016-7606(2000)112<1250:LRTTFD>2.0.CO;2).
- Sobel, E.R., Schoenbohm, L.M., Chen, J., Thiede, R., Stockli, D.F., Sudo, M., Strecker, M.R., 2011. Late Miocene–Pliocene deceleration of dextral slip between Pamir and Tarim: implications for Pamir orogenesis. *Earth Planet. Sci. Lett.* 304, 369–378. <https://doi.org/10.1016/j.epsl.2011.02.012>.
- Sobel, E.R., Chen, J., Schoenbohm, L.M., Thiede, R., Stockli, D.F., Sudo, M., Strecker, M.R., 2013. Oceanic-style subduction controls late Cenozoic deformation of the Northern Pamir orogen. *Earth Planet. Sci. Lett.* 363, 204–218. <https://doi.org/10.1016/j.epsl.2012.12.009>.
- Stearns, M.A., Hacker, B.R., Ratschbacher, L., Lee, J., Cottle, J.M., Kylander-Clark, A., 2013. Synchronous Oligocene–Miocene metamorphism of the Pamir and the north Himalaya driven by plate-scale dynamics. *Geology* 41, 1071–1074. <https://doi.org/10.1130/G34451.1>.
- Stearns, M.A., Hacker, B.R., Ratschbacher, L., Rutte, D., Kylander-Clark, A.R.C., 2015. Titanite petrochronology of the Pamir gneiss domes: Implications for middle to deep crust exhumation and titanite closure to Pb and Zr diffusion. *Tectonics* 34, 784–802. <https://doi.org/10.1002/2014TC003774>.
- Stübner, K., Ratschbacher, L., Rutte, D., Stanek, K., Minaev, V., Wiesinger, M., Gloaguen, R., Project TIPAGE members, 2013a. The giant Shakh-dara migmatitic gneiss dome, Pamir, India–Asia collision zone: 1. Geometry and kinematics. *Tectonics* 32, 948–979. <https://doi.org/10.1002/tect.20057>.
- Stübner, K., Ratschbacher, L., Weise, C., Chow, J., Hofmann, J., Khan, J., Rutte, D., Sperner, B., Pfänder, J.A., Hacker, B.R., Dunkl, I., Tichomirowa, M., Stearns, M.A., Project TIPAGE members, 2013b. The giant Shakh-dara migmatitic gneiss dome, Pamir, India–Asia collision zone: 2. Timing of dome formation. *Tectonics* 32, 1404–1431. <https://doi.org/10.1002/tect.20059>.
- Tang, G., Wyman, D.A., Wang, Q., Yin, J., Dan, W., 2022. Long-distance lateral magma propagation and Pamir Plateau uplift. *Geophys. Res. Lett.* <https://doi.org/10.1029/2021gl096467>.
- Thiede, R.C., Sobel, E.R., Chen, J., Schoenbohm, L.M., Stockli, D.F., Sudo, M., Strecker, M.R., 2013. Late Cenozoic extension and crustal doming in the India–Eurasia collision zone: new thermochronologic constraints from the NE Chinese Pamir. *Tectonics* 32, 763–779. <https://doi.org/10.1002/tect.20050>.
- Villarreal, D.P., Robinson, A.C., Carrapa, B., Worthington, J., Chapman, J.B., Oimahmadov, I., Gadoev, M., MacDonald, B., 2020. Evidence for late Triassic crustal suturing of the Central and Southern Pamir. *J. Asian Earth Sci.* X 3, 100024. <https://doi.org/10.1016/j.jaesx.2019.100024>.

- Weather China, 2020. Climatic Data for Tashkurgan County (1971–2000). <http://www.weather.com.cn/cityintro/101130903.shtml>.
- Willett, S.D., McCoy, S.W., Perron, J.T., Goren, L., Chen, C., 2014. Dynamic reorganization of river basins. *Science* 343, 1248765. <https://doi.org/10.1126/science.1248765>.
- Wobus, C., Whipple, K.X., Kirby, E., Snyder, N., Johnson, J., Spyropolou, K., Crosby, B., Sheehan, D., 2006. Tectonics from topography: Procedures, promise, and pitfalls. *Spec. Paper Geol. Soc. Am.* 398, 55–74. [https://doi.org/10.1130/2006.2398\(04\)](https://doi.org/10.1130/2006.2398(04)).
- Worthington, J.R., Ratschbacher, L., Stübner, K., Khan, J., Malz, N., Schneider, S., Kapp, P., Chapman, J.B., Goddard, A.S., Brooks, H.L., Lamadrid, H.M., Steele-MacInnis, M., Rutte, D., Jonckheere, R., Pfander, J., Hacker, B.R., Oimahmadov, I., Gadoev, M., 2020. The Alichur dome, South Pamir, Western India–Asia collisional zone: Detailing the Neogene Shakh dara–Alichur syn-collisional gneiss-dome complex and connection to lithospheric processes. *Tectonics* 39. <https://doi.org/10.1029/2019tc005735> e2019TC005735.
- Wu, Y., Yang, R., He, J., Chen, H., Lin, X., Shi, X., An, K., Li, C., Gao, S., Chen, Y., 2023. Characteristics of landscape and erosion in the Eastern Pamir and their implications for regional fault connections. *Geomorphology* 441, 108916. <https://doi.org/10.1016/j.geomorph.2023.108916>.
- Xu, Q., Zhao, J., Yuan, X., Liu, H., Ju, C., Schurr, B., Bloch, W., 2021. Deep crustal contact between the Pamir and Tarim Basin deduced from receiver functions. *Geophys. Res. Lett.* 48 <https://doi.org/10.1029/2021GL093271> e2021GL093271.
- Yin, A., Harrison, T.M., 2000. Geologic evolution of the Himalayan–Tibetan orogen. *Annu. Rev. Earth Planet. Sci.* 28, 211–280. <https://doi.org/10.1146/annurev.earth.28.1.211>.